

UI

(NASA-TM-82476) THE MARSHALL SPACE FLIGHT
CENTER KC-135 ZERO GRAVITY TEST PROGRAM FOR
FY 1981 (NASA) 69 p HC A04/MF A01 CSCL 11G

N82-26350

Unclas
G3/12 28122

NASA TECHNICAL MEMORANDUM

NASA TM-82476

THE MARSHALL SPACE FLIGHT CENTER KC-135 ZERO GRAVITY
TEST PROGRAM FOR FY1981

R. E. Shurney, Editor
Systems Analysis and Integration Laboratory

March 1982



NASA

*George C. Marshall Space Flight Center
Marshall Space Flight Center, Alabama*

1. REPORT NO. NASA TM-82476		2. GOVERNMENT ACCESSION NO.		3. RECIPIENT'S CATALOG NO.	
4. TITLE AND SUBTITLE The Marshall Space Flight Center KC-135 Zero Gravity Test Program for FY1981				5. REPORT DATE March 1982	
				6. PERFORMING ORGANIZATION CODE	
7. AUTHOR(S) Edited by R. E. Shurney				8. PERFORMING ORGANIZATION REPORT #	
9. PERFORMING ORGANIZATION NAME AND ADDRESS George C. Marshall Space Flight Center Marshall Space Flight Center, AL 35812				10. WORK UNIT NO.	
				11. CONTRACT OR GRANT NO.	
12. SPONSORING AGENCY NAME AND ADDRESS National Aeronautics and Space Administration Washington, D.C. 20546				13. TYPE OF REPORT & PERIOD COVERED Technical Memorandum	
				14. SPONSORING AGENCY CODE	
15. SUPPLEMENTARY NOTES Prepared by Systems Analysis and Integration Laboratory, Science and Engineering					
16. ABSTRACT <p>During FY81, researchers from Marshall Space Flight Center (MSFC) conducted seven separate investigations during 23.5 hours of testing aboard the KC-135 zero-gravity aircraft, based at Ellington Air Force Base, Texas. Although this represented fewer hours than initially projected, all experiment objectives were met or exceeded. This Technical Memorandum compiles all results achieved by MSFC users during FY81, a year universally considered to be highly productive.</p> <p>We thank the Aircraft Operations people at Johnson Space Center for their enthusiastic support, this year and in years past.</p>					
17. KEY WORDS Power Ratchet Tool Low Gravity Test Ice Crystal Growth Thermal Wave Experiment High Temperature Casting Furnace			18. DISTRIBUTION STATEMENT Unclassified -- Unlimited		
19. SECURITY CLASSIF. (of this report) Unclassified		20. SECURITY CLASSIF. (of this page) Unclassified		21. NO. OF PAGES 69	22. PRICE NTIS

TABLE OF CONTENTS

	Page
INTRODUCTION	1
I. POWER RATCHET TOOL ZERO-GRAVITY TEST, By V. Kulpa	3
II. MIT SPACE SYSTEMS LAB KC-135 TESTS - FINAL REPORT SUMMARY, By M. Bowden	7
III. JET PROPULSION LABORATORY LOW GRAVITY TESTS CONDUCTED ON THE KC-135, By D. D. Elleman, A. Croonquist, and T. G. Wang	21
IV. GROWTH OF ICE CRYSTALS FROM SALT SOLUTION IN LOW GRAVITY, By Vernon Keller, Robert Owen, and Otha Vaughan, Jr.,	37
V. THERMAL WAVE EXPERIMENT, By B. J. Anderson, Vernon Keller, and David Bowdle	41
VI. OPTICAL MEASUREMENTS AND TESTS PERFORMED IN A LOW-GRAVITY ENVIRONMENT, By Robert B. Owen	47
VII. HIGH TEMPERATURE CASTING FURNACE, By M. H. Johnston	59

PRECEDING PAGE BLANK NOT FILMED

TECHNICAL MEMORANDUM

THE MARSHALL SPACE FLIGHT CENTER KC-135 ZERO GRAVITY TEST PROGRAM FOR FY1981

INTRODUCTION

Since 1959, aircraft flying parabolic trajectories have been used by the National Aeronautics and Space Administration (NASA) and the Department of Defense (DOD) to create cyclic periods of weightlessness within the aircraft cabins. While several aircraft have been and still are being used in this capacity, the specially modified KC-135, based at Ellington AFB, Texas, is the largest and most widely used. This aircraft, which offers 20 to 30 sec of weightlessness per maneuver, features a working volume measuring 60-ft long, 10-ft wide, and 7-ft high. Universal user services include a tiedown grid pattern, special photoflood lighting, and a variety of ac and dc power supplies.

Initially, aircraft-based weightless simulations were employed primarily to test human reaction to zero gravity and to help in the development of crew aids. As we gained extensive experience with actual manned space flight, the aircraft has been increasingly used as a test bed for proposed scientific flight experiments and spacecraft systems. Engineers and scientists observe first-hand the strengths and weaknesses of their designs.

Compiled in this report are papers which collectively document the FY1981 Marshall Space Flight Center (MSFC) KC-135 program. In all cases the papers were prepared by the individuals who proposed the investigations, provided the hardware, and conducted test operations aboard the aircraft. The overall program was coordinated and facilitated by Man/System Integration Branch, EL15.

The editor expresses his sincere thanks to each participant and author whose work is presented herein.

I. POWER RATCHET TOOL ZERO-GRAVITY TEST

By V. Kulpa

INTRODUCTION

In January 1980, NASA's Man/Systems Integration Branch at Marshall Space Flight Center (MSFC) began research work on a Power Ratchet Tool (PRT). A pneumatic ratchet wrench (Sears Model No. 756.18803) used in neutral buoyancy tests on Space Telescope maintenance operations demonstrated an eight to one time savings over a hand operated ratchet wrench. The next step was a PRT Prototype I, a 28 Vdc motor (TRW Globe Motor No. 311A202-8JM) adapted to the Sears pneumatic ratchet wrench drive mechanism (Fig. I-1). Performance tests were conducted in the laboratory to determine the wrench's machine characteristics. The man-machine interactions were studied in zero-g tests aboard the KC-135 aircraft. Even though the PRT Prototype I did not produce the required 300-lb/in. torque (maximum 55 lb/in.), it demonstrated the concept of power ratchet mechanisms for future extra-vehicular maintenance tools.

The importance of zero-g tests cannot be overemphasized. Without gravity, the simplest task can become difficult because of Newton's third law of motion (to every action there is an equal and opposite reaction). The KC-135 aircraft provides 30 sec of zero-g for engineers to study and discover reaction force effects in man-machine systems.

EXPERIMENT DESCRIPTION

Two zero-gravity experiments were conducted to examine PRT operation and man-machine interaction. Experiment 1 measured PRT torque output, while experiment 2 was primarily designed to investigate reaction forces.

Experiment 1 consisted of a test beam (Fig. I-2), torque wrench (Snap-on, 0-150 lb./in.), a 7/16-in. 12-point 3/8-in. square drive socket, and the PRT Prototype I. The PRT and torque wrench are connected via the 7/16-in. socket, and during the zero-g period, power is applied to the wrench and torque reading noted.

Experiment 2 is very similar to experiment 1 except the PRT is used to tighten a fixed 7/16-in. bolt on the test beam (Fig. I-2). During the zero-g period, the PRT is activated and the reaction torque noted. Three different sockets were used: standard 1-in. long 7/16-in. 12-point 3/8-in. square drive socket; 6-in. long 7/16-in. socket; and a 24-in. long 7/16-in. long socket (both 6- and 24-in. lengths also have a 10-degree swivel socket end).

RESULTS

In experiment 1, the torque meter consistently measured 55-lb-in. torque for four trials. Without any type of physical restraint, the subject could control his position because the reaction torque was not as great as expected. The length of

the socket extension in experiment 2 effected both reaction torque and initial positioning of the socket onto the bolt head. Increasing the extension length made it harder for the subject to use his free hand as a brace and reaction force came into play. The positioning task also increased in difficulty with the longer extensions because of the unfamiliar zero-g environment.

CONCLUSION

These preliminary zero-g experiments indicate a need for future power hand tool testing. The two experiments focused on the man-machine interface using the test subjects comments for data.

Preliminary tests indicate that the power ratchet mechanism produces reaction torques that the user can control if provided some type of brace (i.e., foot restraint).

It is recommended that future zero-g power hand tool tests include instruments designed to measure the reaction torque for specific input torque values.

ORIGINAL PAGE
BLACK AND WHITE PHOTOGRAPH

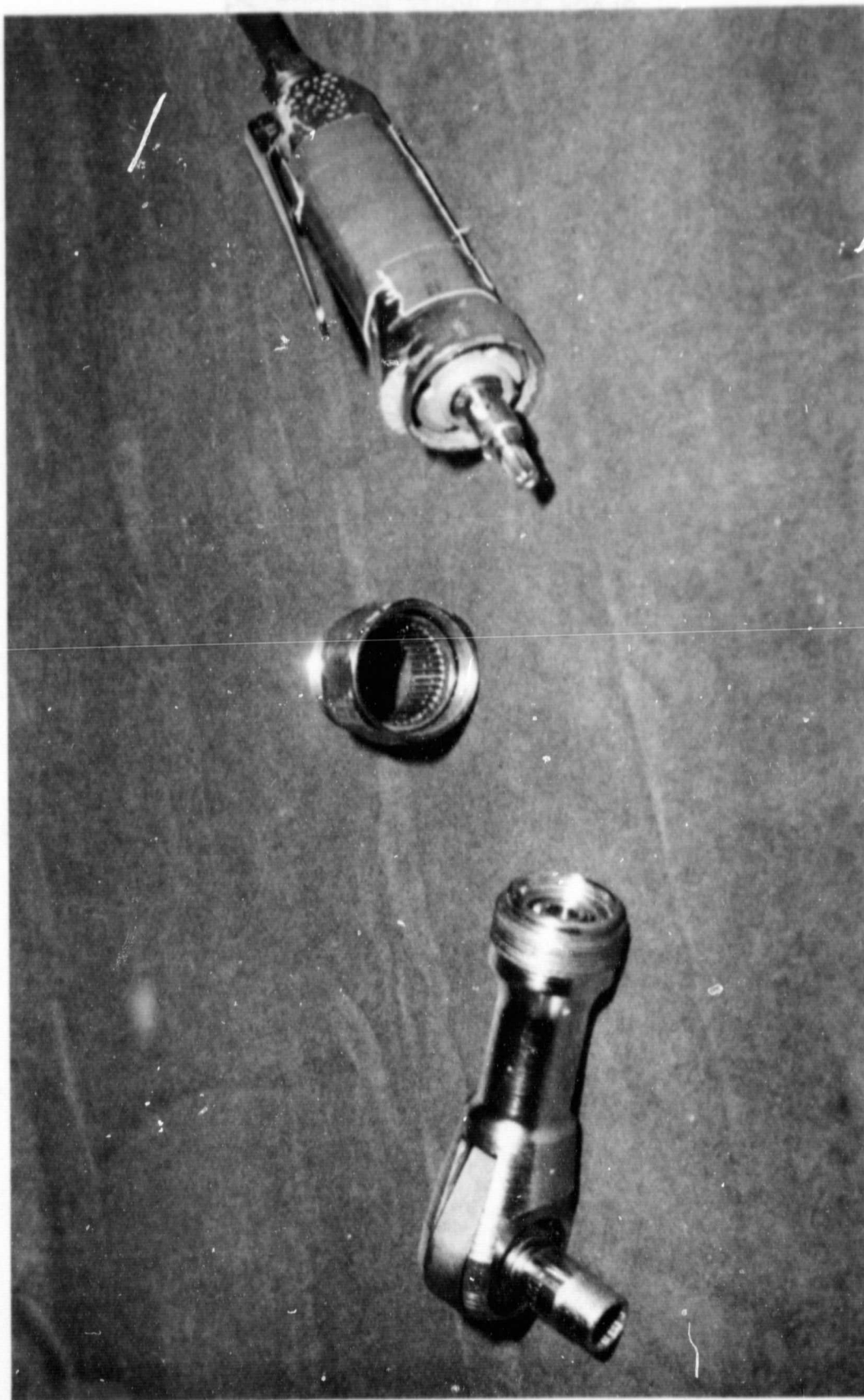


Figure I-1. Power ratchet tool prototype 1, TRW globe motor.



Figure 1-2. Torque wrench (Snap-on).

II. MIT SPACE SYSTEMS LAB KC-135 TESTS - FINAL REPORT SUMMARY

By M. Bowden

INTRODUCTION

There are two primary methods for simulating weightlessness on Earth: neutral buoyancy and parabolic flights. In a neutral buoyancy simulation, all objects in the simulation (including the test subjects) are made neutrally buoyant in water. The experiment is then performed in a large watertank with the test subjects using scuba equipment or wearing pressure suits. The primary drawback to this method is water drag which hinders and damps out all motions underwater. Parabolic flights in a KC-135 aircraft provide brief periods of zero-g. This works very well for small scale experiments which need only relatively short intervals of weightlessness, but does not lend itself to simulating large scale assemblies which may take an hour to complete. Neutral buoyancy is therefore the best simulation available for large space structures assembly tests on Earth.

Ideally, the productivity data obtained in a neutral buoyancy simulation could be applied directly to the on orbit situation, but this is not valid because of the presence of water drag. First determine under what conditions the underwater simulation is a good simulation of space. Then, once these conditions are met, the neutral buoyancy data should be directly applicable. The purpose of this study was to compare assembly dynamics underwater with those expected in space, in an attempt to identify the conditions of validity for neutral buoyancy simulation.

Two aspects of the dynamics of weightless assembly were investigated: body dynamics and beam dynamics. The study of body dynamics was centered around a mathematical model of the human body performing a simple assembly-type motion. This model was validated experimentally using data obtained by a test subject performing the motion in three different environments:

- 1) With water drag, without pressure suit (MIT data)
- 2) With water drag, with pressure suit (MSFC data)
- 3) Without water drag, without pressure suit (KC-135 data).

The model was then used to predict body dynamics expected in space (without water drag, with pressure suits), and a comparison could therefore be made, using just the mathematical model, between neutral buoyancy body dynamics (1 and 2) and in-space body dynamics.

Beam dynamics were investigated using an analog computer simulation of a beam, to which was applied both a force and a moment at one end. The simulation allowed the beam to react first as it would in space (no water drag), and then as it would underwater (with water drag). Use of this simulation yielded learning rates and control laws applicable to a person controlling a beam with and without damping. The mass and moment of inertia of the beam were chosen quite high to represent a structural member that might be used in a large space structure. An experimental test series for beam dynamics was also performed on the KC-135 aircraft to compare the control functions used in true weightlessness with those used in the analog simulation.

This report summarizes only the MIT tests performed in the KC-135 at Johnson Space Center (JSC), but a more complete report can be found in SSL report No. 9-81, "Dynamics of Manual Assembly of Large Space Structures in Weightlessness," and SSL report No. 10-81, "MIT Space Systems Lab KC-135 Tests - Final Report."

BODY DYNAMICS

Mathematical Model

In order to compare the dynamics of a human body underwater with that which would occur in space, a very simple assembly-type motion was chosen and modeled analytically. The motion was that of bringing two masses together at arms' length in front of the chest. This motion results in a tiltback reaction of the test subject, since the center of mass of the system must remain stationary. Underwater, water drag acts against the tiltback motion by resisting torso and leg movement, but it also provides extra thrust to the motion by acting on the arms and test masses. It is not clear which of these two effects predominate, and in fact this depends on the size of the test masses and the way in which they are moved through the water. The mathematical model is a computer program that uses experimentally obtained data on arm motion to predict what the tiltback motion should be. This is then compared with the measured tiltback to see if the model is accurate.

Verification of the Math Model

The mathematical model was verified experimentally in its third environment (without pressure suit, without drag) at NASA JSC on the KC-135 aircraft.

Experimental Hardware

A harness was used to restrain the test subject and to mount the instruments on (Fig. II-1). Potentiometers were used over each shoulder to measure arm angle. Two rate gyroscopes were used to measure the tiltback velocity which could then be integrated to get tiltback angle.

The test masses in this experiment were two sets of standard weightlifting dumbbells: one pair of 8-kg masses and one pair of 16-kg masses.

Experimental Procedure

This series of body dynamics tests was performed during approximately 36 parabolas. Each of two test subjects performed the arm motion with empty hands (6 parabolas), with the small test masses (6 parabolas). The first two parabolas in every series of six were slow runs, then two parabolas of medium speed runs, then two of fast runs. During each parabola, as many runs as possible were performed at the appropriate speed.

Experimental Results

To analyze this data, signals from the pots (θ) and gyros ($\ddot{\alpha}$) were digitized. The tiltback angle (α) was obtained by integrating $\ddot{\alpha}$ on the analog computer and then digitizing this signal as well. As a result, recordings of θ , α , and $\dot{\alpha}$ were available

for every run. Fifth order polynomials were fitted to the theta data so that it could be input as a smooth curve into the mathematical model. In addition, the initial value of $\dot{\alpha}$, tiltback velocity, was used in the model to start the run off with the same initial velocity that was experienced in reality.

In the Appendix, graphs of arm angle, tiltback, and tiltback velocity are plotted for a representative sample of the runs. Experimental points for tiltback and tiltback velocity (x) are superimposed on the predicted curves. The agreement between the experimental data and the predicted curves is excellent. In general, both the α and $\dot{\alpha}$ curves fall right among the experimental points and show precisely the same shape.

Table II-1 shows the final values of tiltback predicted by the model and experimental tiltback for all of the runs analyzed which were not rejected because of experimental error. The agreement is quite good; the difference between the two final angles is on the order of a few degrees in general, which represents about 20 percent of the tiltback angle. The trend of having higher tiltback angles for larger test masses is substantiated by this data. It is interesting to note also that the final tiltback angles experienced here are, in general, much greater than those experienced underwater. This data validates very well the mathematical model of the human body in weightlessness without water drag.

Body Dynamics - Conclusions

Evaluation of Model

Experimental results obtained at MIT, at MSFC, and in the KC-135 validate the mathematical model of a person performing an assembly motion in the following three configurations:

- 1) With water drag, without pressure suit (MIT)
- 2) With water drag, with pressure suit (MSFC)
- 3) Without water drag, without pressure suit (KC-135).

Both the inertial section of the model and the section relating to water drag have therefore been verified. Consequently, it is now permissible to use the model to predict body dynamics in a fourth configuration, without water drag, with pressure suit. This represents what one would expect to happen in space, in an on-orbit construction job, for example.

Comparison of Neutral Buoyancy with Space

As explained above, one can use the mathematical model to compare body dynamics in neutral buoyancy, with those expected in the fourth configuration, space. Figure II-2 shows a graph of final tiltback angle as a function of test mass, for test masses from 0 to 200 kg.

The two curves show the greatest difference for small test masses and seem to converge or stay very close for large masses. This is reasonable, because for small masses, the drag terms predominate, while for large masses, the inertial terms are far more important in the equations. The two curves cross over at approximately 125 kg which represents about 60 percent of the body mass underwater. At this

point, theoretically, the neutral buoyancy simulation should be a very good simulation of space, because the dynamics in the two environments are identical. In practice, this means that to insure a good neutral buoyancy simulation, one should try to work with masses as large as possible underwater. A good large space structures neutral buoyancy test, in which the dynamics are similar to space within 20 percent, would involve beams or other structural hardware that mass around 25 percent or greater of the test subject's mass.

BEAM DYNAMICS

Introduction

The purpose of this section of the study is to investigate the dynamics of a beam alone. The beam represents a structural member of a space structure that is being manually assembled. It is assumed that a force and a moment must be applied at one end of the beam to line it up so that it can be locked into place on the structure. Neutral buoyancy and weightlessness are compared in this case by studying the manner in which a test subject controls a beam (phase planes and time histories of control inputs) and the learning rates established with and without drag. This system, being much less complex than that of the body, was studied in two forms only. First, a simulation of a beam with two degrees of freedom (translation and rotation) was set up on the analog computer, so that it could model the dynamics both with water drag terms and without. Then, data from a KC-135 experiment was analyzed in order to compare the control functions used in true weightlessness to those used for the analog simulation. Only the KC-135 experiment will be described here.

KC-135 Beam Dynamics

The intent of this experiment was to set up a high moment of inertia beam that could be rotated about one end to study the problem of controlling a beam in weightlessness. One of the most important parts of this problem is the question: How important are foot restraints at a work station where a space construction worker is assembling beams?

Experimental Hardware

The beam used in this experiment was simply a 6-ft long aluminum tube, 1 in. in diameter. The moment of inertia of the beam was determined by sliding heavy disks of various sizes on one end of the beam. The other end of the beam was attached to a camera mount at about chest height (Fig. II-3). A set of standard NASA foot restraints were installed in such a way that a person standing in them could comfortably have one hand on the camera mount and the other hand on the beam.

Data for this experiment was collected using two of the instruments described previously. The potentiometer at the interface between the beam and the camera mount measured beam angle. A rate gyroscope was taped to the beam about a foot down from the axis of rotation. This measured the angular velocity as the beam was rotated.

Test Procedures

Each of two test subjects tried three parabolas in foot restraints and three parabolas out of foot restraints for a low moment of inertia beam (16 kg × 6 ft), and then repeated the same with a high moment of inertia beam (32 kg × 2 m). For each parabola, the procedure was to lift the beam so that it was perpendicular to the camera mount, and then to rotate it back and forth in a plane parallel to the floor of the aircraft. Control of the beam was tested by requiring that it be repeatedly lined up with a mark on the wall of the plane, and then rotated and stopped along the centerline of the plane.

Experimental Results

The data obtained in this experiment was analyzed by first digitizing the signals recorded on tape for beam angle and angular velocity. It quickly became apparent from looking at these numbers that the signal from the potentiometer was intermittent and, therefore, unusable. Fortunately, the signal from the gyroscope was clear enough that it could be integrated to give a value for the beam angle during the run.

Using this method for obtaining the beam angle (θ) and beam velocity ($\dot{\theta}$), a phase plane of the motion during a parabola could be drawn. This was done for one test in Figure II-4. The curves in this case and for all of the parabolas that were looked at are very noisy. This is primarily caused by the fact that the beam could not be swung parallel to the floor of the plane, because as the parabola proceeded, the aircraft pitched forward continuously under the beam. As a result, the beam had a tendency to bump the floor, walls, and equipment during the run.

Despite the noisy signal from the gyro, the phase planes do show that some of the characteristic shapes occur in these curves. For example, both runs show a parabolic section in which a constant deceleration was attempted to stop the beam at its final location (arrows). There is some overshoot in both cases, but not all that much ($\pm 5^\circ$). According to these phase planes, the task was accomplished fairly well and efficiently, despite the lack of damping.

The question of the usefulness of foot restraints was only partially answered by this experiment. At first, it appeared that performing the task in foot restraints was imperative. The first time it was tried without the foot restraints, the test subject's feet hit the ceiling and the beam bounced off the floor while rotating. However, only two parabolas later, the test subject had instinctively adapted to the new dynamics of the situation well enough to be able to control the beam. The performance was not as accurate as in foot restraints, but the potential was there because the learning was so high. The most difficult part was trying to keep the beam level while the plane pitched forward, but this was accomplished to some extent by holding onto the camera mount with the right shoulder and arm and applying leverage in that manner. Thus, although the task seemed much easier with foot restraints, it was possible, with a little experience, to do it without, almost as accurately.

Conclusion

The analog simulation of beam dynamics yielded the following conclusions on the difference between neutral buoyancy and true weightlessness.

Controlling a beam without damping requires more careful attention and more frequent changes of force and moment input than controlling the same beam with damping. Test subjects, in general, felt that the without-drag simulation was more difficult and tiring.

A phase plane study of the controlling algorithms shows that overshoot is more of a problem without drag. The total time to complete the operation, however, is not usually longer, in part because the response without drag is slightly faster than that with drag.

The KC-135 beam dynamics experiment showed that a high moment of inertia beam can be controlled without damping, and for a beam of identical moment of inertia and shape, the task is probably harder underwater because of the drag forces. Foot restraints can be foregone if some time is spent learning the dynamics of operating without them.



Figure II-1. KC-135 body dynamics.

ORIGINAL PAGE
BLACK AND WHITE PHOTOGRAPH

ORIGINAL PAGE IS
OF POOR QUALITY

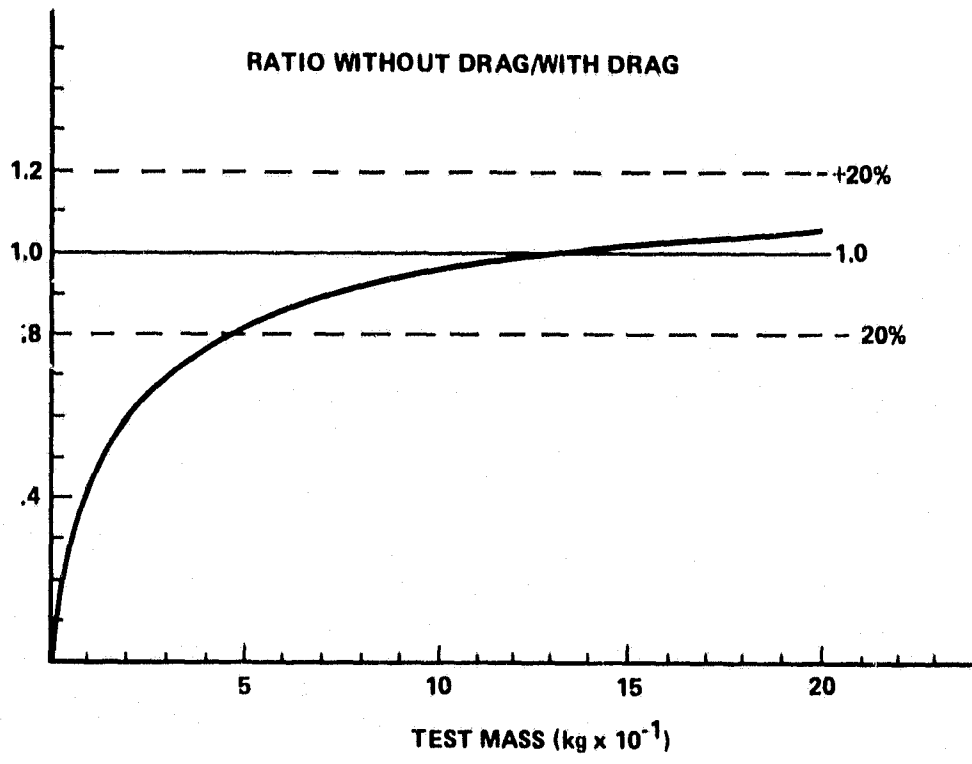
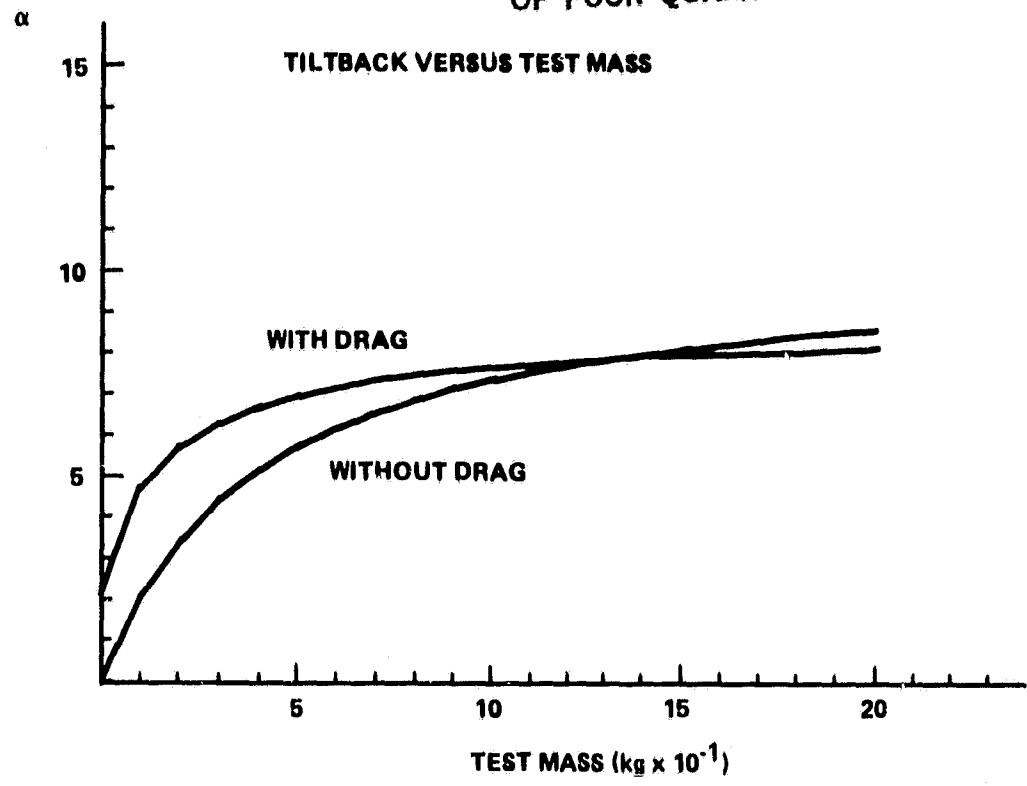


Figure II-2. Tiltback versus test mass with and without drag.

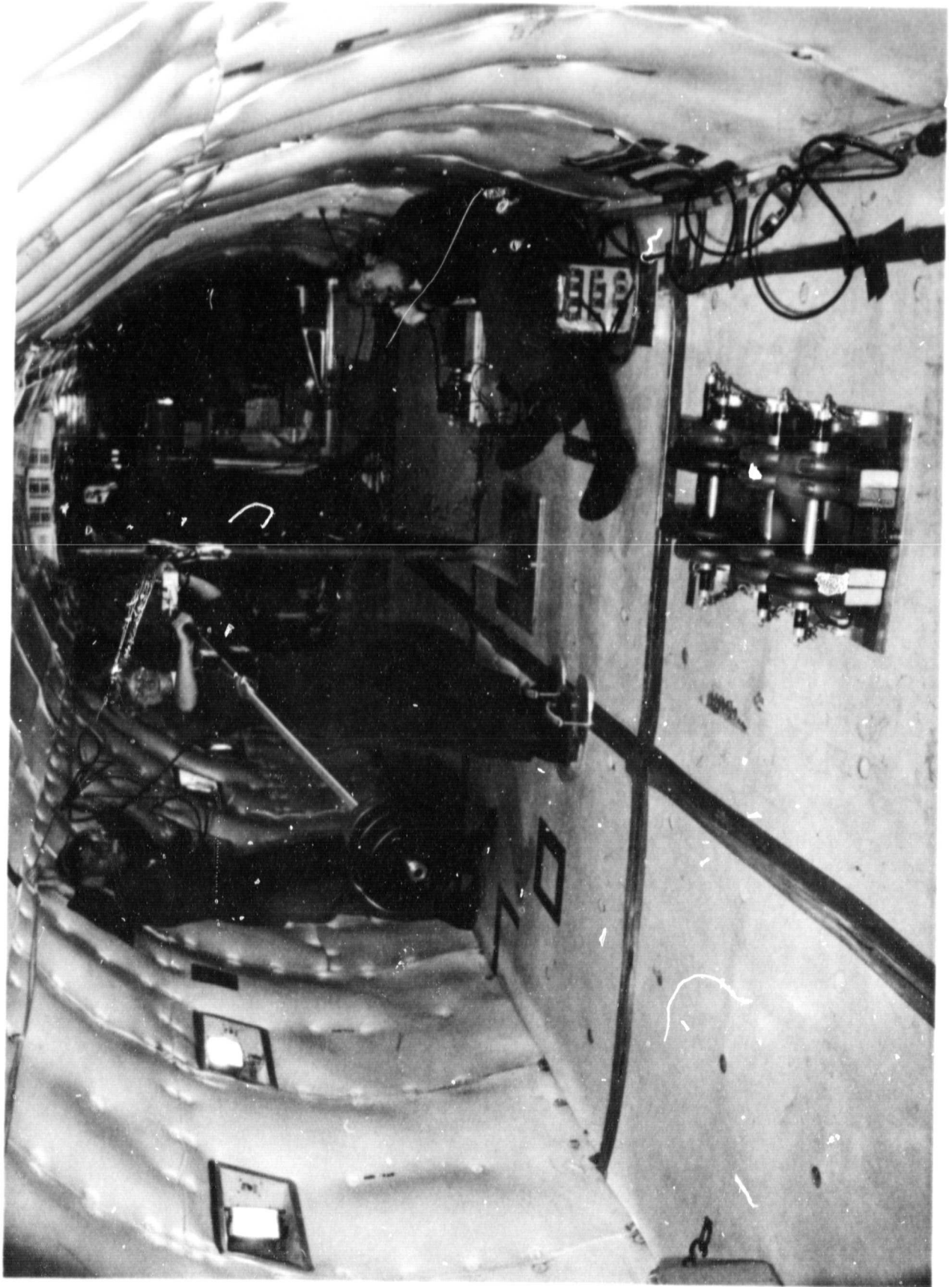


Figure II-3. KC-135 beam dynamics.

ORIGINAL PAGE
BLACK AND WHITE PHOTOGRAPH

ORIGINAL PAGE IS
OF POOR QUALITY

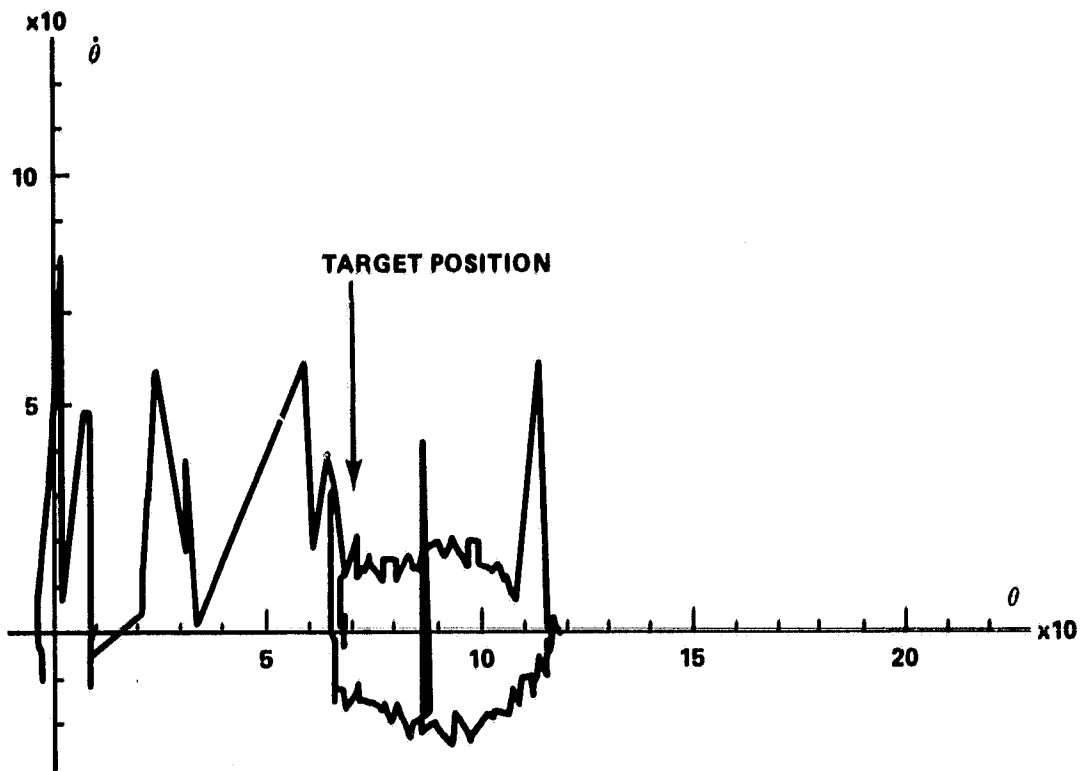


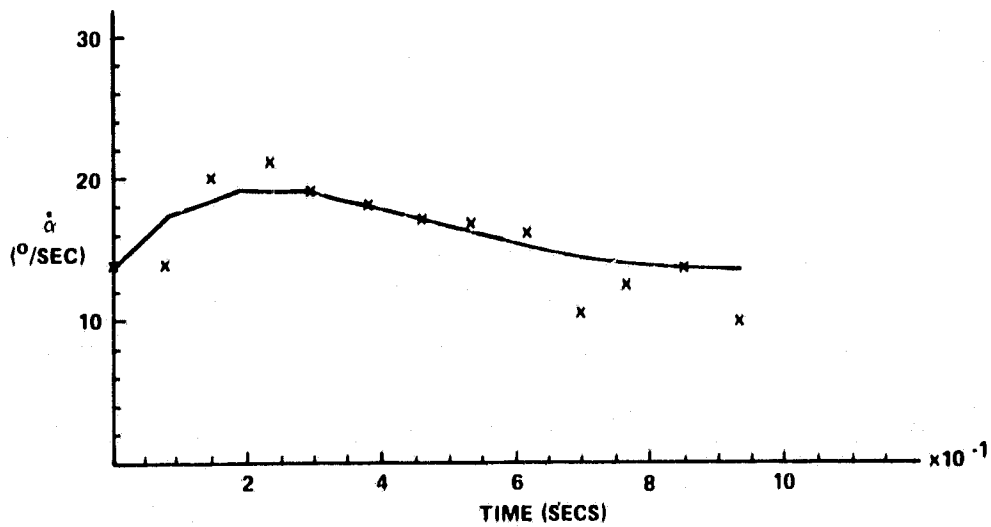
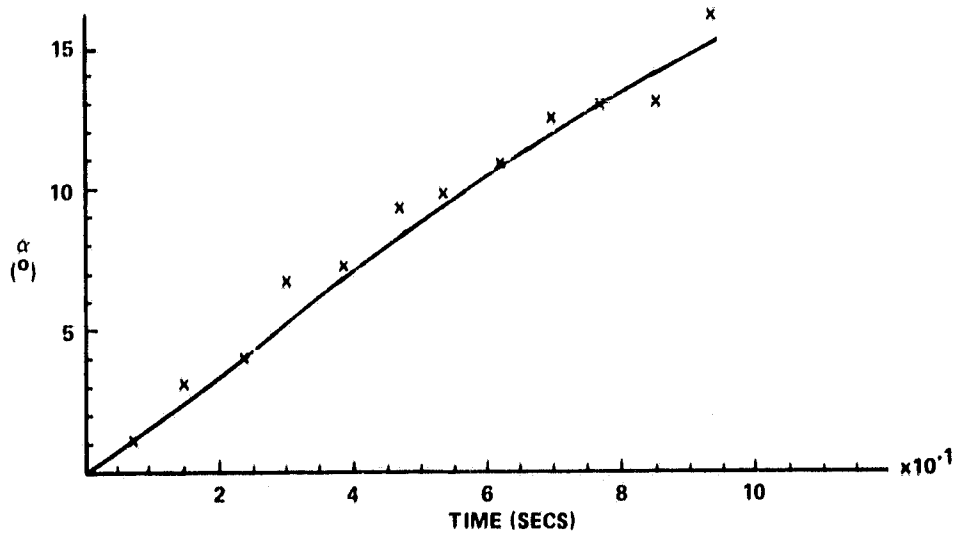
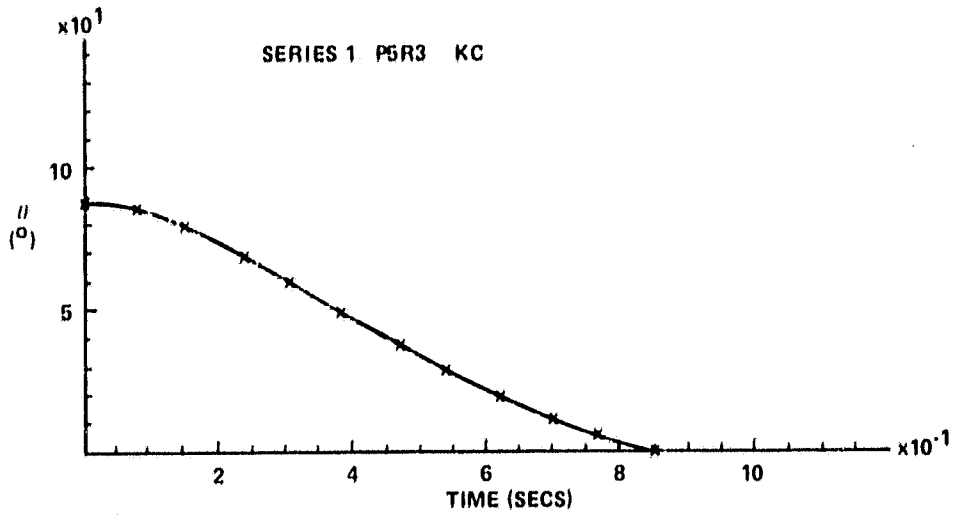
Figure II-4. Phase plane for KC-135.

TABLE II-1. KC-135 BODY DYNAMICS DATA

Series	Run	α Predicted	α Experimental	Difference	Runtime
1	1	26.46	23.42	-3.04	1.62
	2	28.26	24.45	3.81	1.53
	3	19.40	15.09	-4.31	1.08
	4	11.06	11.45	0.39	1.07
	5	10.84	15.09	4.25	1.00
	6	12.63	13.53	0.90	1.00
	7	15.24	16.13	0.89	0.93
	8	6.96	6.25	-0.71	0.85
2	1	18.78	12.49	-6.29	1.62
	2	18.12	11.44	-6.68	1.62
	3	20.06	17.69	-2.37	1.70
	4	18.44	23.94	5.50	1.47
	5	48.44	40.06	8.38	1.38
	6	38.91	38.50	0.41	1.07
	7	8.37	11.96	3.59	1.00
	8	17.89	15.09	-2.80	0.70
3	1	80.26	57.76	-22.50	2.53
	2	49.33	43.18	-6.15	2.38
	3	15.15	8.84	-6.31	1.47
	4	35.91	29.14	-6.77	1.47
	5	55.21	32.26	-22.95	1.15
	6	36.16	21.86	-14.30	1.00
	7	44.24	34.87	-9.37	1.00

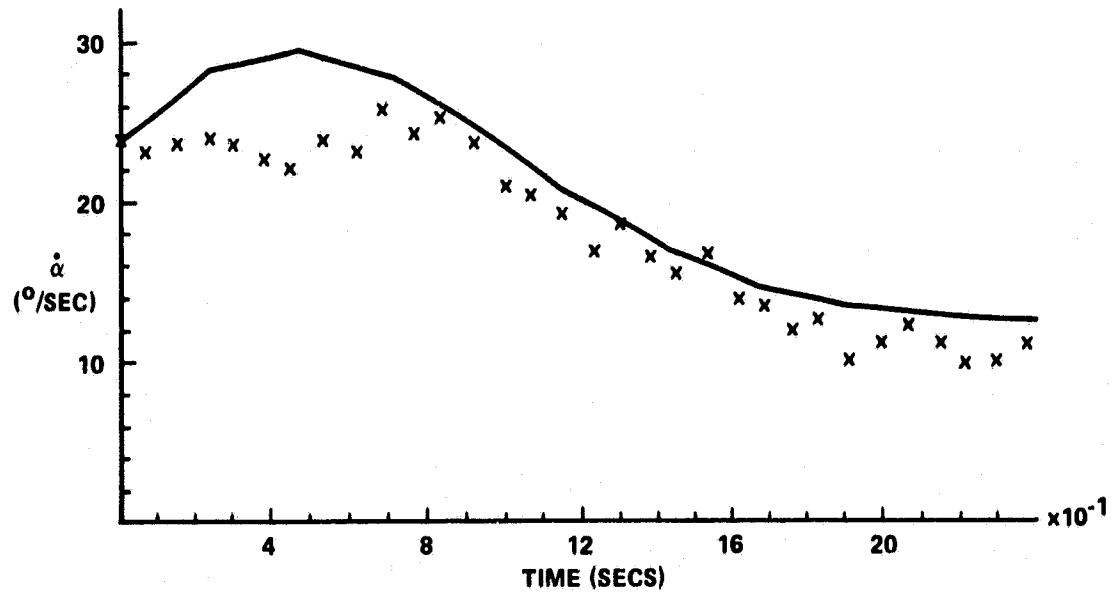
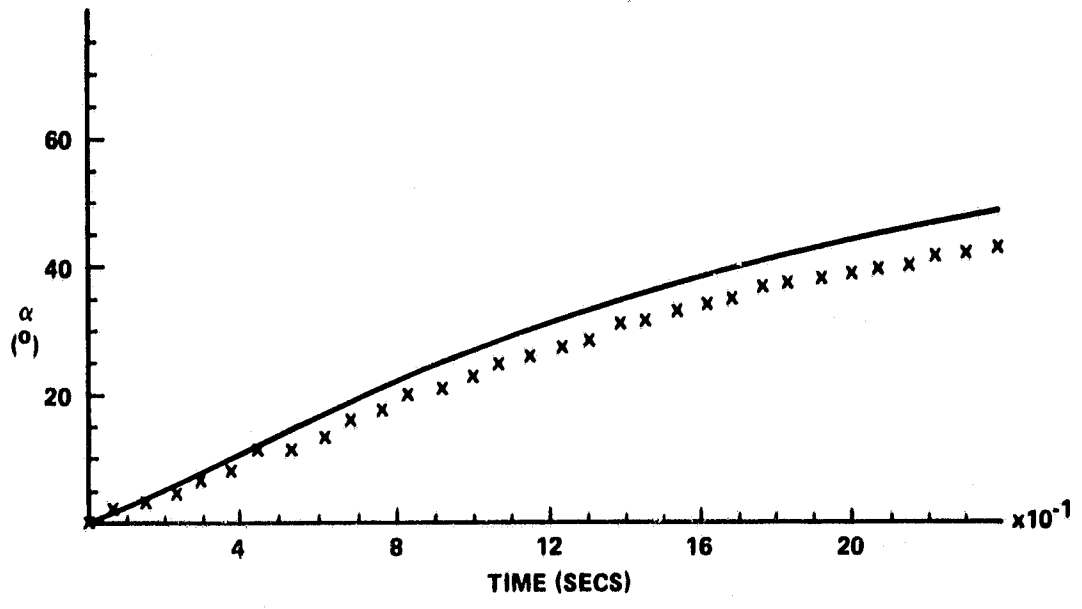
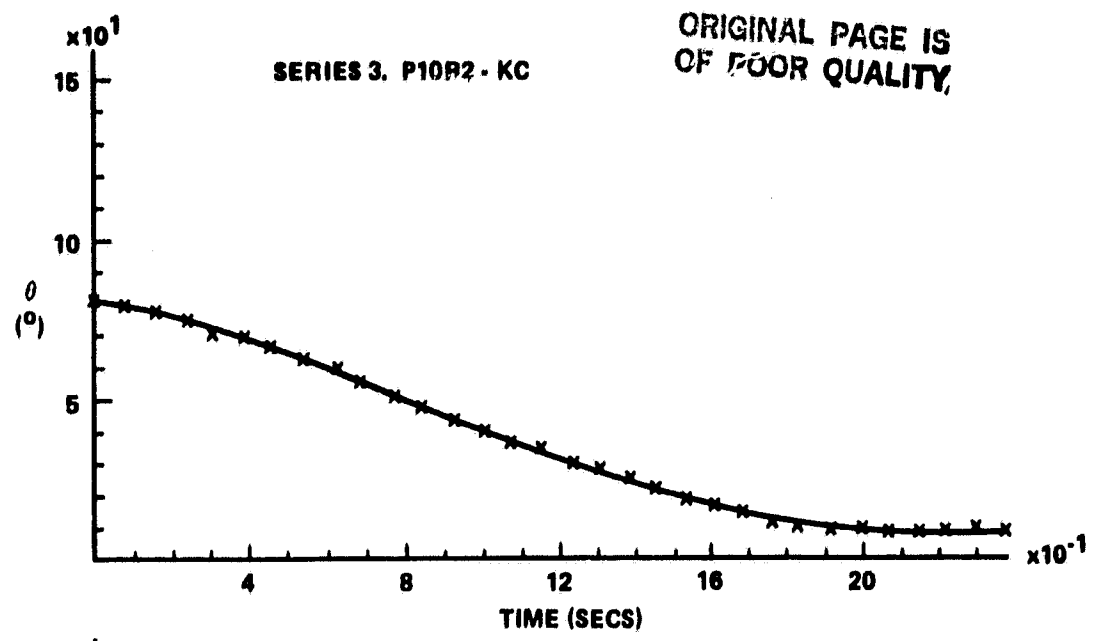
APPENDIX

KC-135 BODY DYNAMICS DATA



ORIGINAL PAGE IS
OF POOR QUALITY,

SERIES 3. P10R2 - KC



III. JET PROPULSION LABORATORY LOW GRAVITY TESTS CONDUCTED ON THE KC-135

D. D. Elleman, A. Croonquist, and T. G. Wang

The Jet Propulsion Laboratory (JPL) has conducted a series of tests on the JSC Reduced Gravity Aircraft in conjunction with the MSFC SPAR program. These tests were conducted to demonstrate experiment feasibility, operation of the three axis acoustic module prototype subsystems used in the SPAR flights, and instrument calibration.

The primary objectives of the projected JPL SPAR flight 77-18 are: the study of the rotation induced bubble centering of a liquid drop rotated in an acoustic positioning device; investigation and demonstration of bubble centering of a liquid shell undergoing oscillation in its various normal modes; and the study of bubble centering of a liquid shell which allowed to undergo expansion induced instability of the liquid shell. The primary objectives of the SPAR 76-20 experiments are: an experimental verification of the predicted shapes of a rotating liquid drop; measurement of the mixing effects generated by spin-up and spin-down processes; and measurement of surface waves on a rotating drop fission and measurement of the Bohr-Wheeler Saddle Point of a rotating drop.

To date the JPL SPAR experiments have been conducted using ultra pure water as the liquid in the drop experiments. The liquid of choice for future SPAR flights is silicone oil, which provides the ability to select a wide variety of viscosities for the test fluid. However, the silicone oil tends to wet, that is, have a small contact angle with most material and this makes deployment of the oil into the acoustic chambers quite difficult. A series of tests on non-wetting treatments of the injection tips with a Fluorad Antimigration coating material, FC-721, was initiated this year. The results of these tests indicate that this treatment of the injection system will allow the deployment of silicone oil for future tests.

A theoretical development of the normal modes of oscillation of a compound drop was completed at JPL (Appendix A). The results of this theory were verified on flights of the KC-135, both the bubble mode and sloshing mode for $n=2$ were observed. The accuracy of the drop oscillation frequency measured on the KC-135 is limited to approximately ± 10 percent of the predicted value due to the short duration of reduced gravity and because of inaccuracy in the diameter of the drop and the bubble. However, these KC-135 experiments allow a calibration to be made as to the frequency range over which the SPAR module must be swept so that accurate measurement of the normal modes can be made.

Rotating drop experiments have been conducted with the three-axis acoustic chamber on the KC-135. A bifurcation point was observed at an angular velocity of approximately $\Omega_s \approx 0.65$ measured in units of $(8\sigma/\rho a^3)^{1/2}$ where the drop passed from that of axisymmetrical shape to that of triaxial. This is close to the predicted value of 0.584 for Ω_s . Some caution must be taken though in putting too much significance to this data in that differential rotation of the drop was undoubtedly present. The differential rotation results from the rapid spinup of the drop that is required because of the short zero gravity time that is available and because of the low viscosity of the liquid used for the drop, water in this case. Future experiments on the SPAR rocket where zero gravity of over 4 min will alleviate this problem.

One of the problems that we have had in the past with conducting rotation experiments with the acoustic positioning module was that the primary method of control of the torque on the sample was by varying the amplitude of the acoustic field. A new technique for control of the torque has been devised and uses complementary modulation. There are two methods of using the complementary modulation, the (-90 to +90 degrees) and the (0-180 degrees) techniques. For rotation the (-90 to +90) degrees) method is used. For zero torque the - and + mode are turned on for equal times, for a + direction torque the + mode is on for a longer period than the - mode. The longer the duty cycle for the + mode, the greater the net average torque in the + direction. Tests to date have been conducted with a 30 Hz duty cycle for equal + and - modes with zero torque on the sample.

Further tests will be conducted on actual rotation of the sample in FY 82.

APPENDIX A

DYNAMICS OF COMPOUND DROPS*

M. Saffren, D. D. Elleman, and W. K. Rhim
Jet Propulsion Laboratory
California Institute of Technology
4800 Oak Grove Drive
Pasadena, California 91109

* The research described in this paper was carried out by the Jet Propulsion Laboratory, California Institute of Technology, under contract with the National Aeronautics and Space Administration.

ABSTRACT

In this paper, normal modes of oscillating compound drops are identified and explicit expressions of their frequencies and boundary motions are presented. The fluids are assumed to be inviscid, incompressible, and the core and the shell to be concentric. Comparison made with experimental results obtained in a neutral buoyancy tank, as a special case, showed good agreement with the theory.

This letter is the first in a series of reports on the study of the dynamics of compound drop systems. Aside from its interest as a fundamental study of compound drops this work can be applied to the fabrication of inertial fusion target pellets, development of containerless materials processing techniques both terrestrial and extraterrestrial, and development of techniques for liquid drop control for fundamental studies in other scientific disciplines such as superfluid drop dynamics.

As shown in Figure 1, the systems consist of three fluids: a host fluid infinite in extent, surrounding a second fluid in the form of a shell, which in turn surrounds a third, the core fluid. The underlying assumptions of the present theory are (i) the density of fluids and the interfacial tensions are arbitrary, (ii) the fluids are incompressible, (iii) they are inviscid, (iv) the equations of fluid motions are linearized to the lowest order of nonlinearity that yields normal modes, and (v) the fluid boundaries are concentric. The conditions (iii) and (v) may be relaxed in ensuing reports.

The equations of motion for the system are well known and are given, in spherical coordinates, as:

$$\nabla^2 \psi = 0 \quad (1)$$

$$\frac{\partial \mathbf{R}}{\partial t} = \left(\hat{\mathbf{r}} - \frac{\bar{\nabla}_s \mathbf{R}}{R} \right) \cdot \bar{\nabla} \psi \quad (2)$$

$$\sigma \bar{\nabla}_s \cdot \hat{\mathbf{n}} = -\Lambda \left[\rho \frac{\partial \psi}{\partial t} + P - \rho (\bar{\nabla} \psi)^2 \right] \quad (3)$$

The first equation for the velocity potential in each fluid follows from the assumption of incompressibility. The second equation is also kinematic and relates the motion of boundaries to the fluid velocity. The equation of the boundary is given as $\mathbf{r} = R(\theta, \phi, t)$. In equation (2) $\hat{\mathbf{r}}$ is a unit vector which points from the origin to the point $R(\theta, \phi)$ on the boundary, and $\bar{\nabla}_s = \theta \partial / \partial \theta + (\hat{\phi} / \sin \theta) \partial / \partial \psi$. Equation (3) is a

dynamic equation indicating that the stress across an interface depends solely on its interfacial tension σ . Here \hat{n} is the unit vector normal to the surface and p denotes the pressure in the resting system.

For a compound drop under dynamic conditions, the boundaries are nearly spherical. The pressure difference across a boundary of radius, \bar{R} , and interfacial tension, σ , is therefore given by

$$\Delta P = - \frac{2\sigma}{\bar{R}} \quad . \quad (4)$$

Linearizing equations (2) and (3) by retaining only those terms which are linear in ψ and R gives

$$\frac{\partial R}{\partial t} - \frac{\partial \psi}{\partial r} = 0 \quad , \quad (2a)$$

and

$$\Delta(\rho \frac{\partial \psi}{\partial t}) = \frac{\sigma}{\bar{R}^2} (2 - L^2) \Delta R \quad , \quad (3a)$$

where L^2 is the surface Laplacian, and $\Delta R = R - \bar{R}$. In this approximation the equations of motion agree with those obtained elsewhere⁽¹⁾ for a less general condition.

Since ψ is a non-singular solution of the Laplace equation, it can be expressed in each region of the system as

$$\psi(\underline{r}, t) = \sum_{\ell, m} [A(\ell, m; t)r^\ell + B(\ell, m; t)r^{-(\ell+1)}] Y_{\ell m}(\theta, \phi) \quad (5)$$

$$\psi_i(\underline{r}, t) = \sum_{\ell, m} A_i(\ell, m; t)r^\ell Y_{\ell m}(\theta, \phi) \quad , \quad (6)$$

$$\psi_o(\underline{r}, t) = \sum_{\ell, m} B_o(\ell, m; t) r^{-(\ell+1)} Y_{\ell m}(\theta, \phi) \quad (7)$$

Also, the inner and outer boundary surfaces can be expressed as

$$\begin{aligned} R \begin{Bmatrix} i \\ o \end{Bmatrix}(\theta, \phi; t) &= \bar{R} \begin{Bmatrix} i \\ o \end{Bmatrix} + \Delta R \begin{Bmatrix} i \\ o \end{Bmatrix}(\theta, \phi; t) \\ &= \bar{R} \begin{Bmatrix} i \\ o \end{Bmatrix} + \sum_{\ell, m} \delta R \begin{Bmatrix} i \\ o \end{Bmatrix}(\ell, m; t) Y_{\ell m}(\theta; \phi) \end{aligned} \quad (8)$$

If we substitute these expressions into equations (2a) and (3a), we show that the equations can be reduced to an eigenvalue equation that can be expressed in a matrix form as

$$\begin{bmatrix} \frac{cm_i}{3} & 1 \\ \tau & \frac{m_o \tau^3}{\sigma} \end{bmatrix} \begin{bmatrix} \Lambda_o \\ \Lambda_i \end{bmatrix} = -\frac{J}{W} \begin{bmatrix} \ddot{\Lambda}_o \\ \ddot{\Lambda}_i \end{bmatrix} \quad (9)$$

where

$$\sigma = \sqrt{\sigma_o / \sigma_i} \quad , \quad \Lambda_o \equiv \sqrt{\sigma \delta} R_o \quad , \quad \Lambda_i \equiv \delta R_i / \sqrt{\sigma} \quad , \quad (10a, b, c)$$

$$m \begin{Bmatrix} o \\ i \end{Bmatrix} = (1 + \tilde{\Delta} \rho \begin{Bmatrix} o \\ i \end{Bmatrix}) \tau^{(2\ell+1)} - \tilde{\Delta} \rho \begin{Bmatrix} o \\ i \end{Bmatrix} \tau^{-(2\ell+1)} \quad , \quad (11)$$

$$\tilde{\Delta} \rho_i = \frac{(\ell + 1)(\rho_i - \rho)}{(2\ell + 1)\rho} \quad , \quad \tilde{\Delta} \rho_o = \frac{\ell(\rho_o - \rho)}{(2\ell + 1)\rho} \quad (12a, b)$$

$$J = (1 + \tilde{\Delta} \rho_o)(1 + \tilde{\Delta} \rho_i) \tau^{(2\ell+1)} - \tilde{\Delta} \rho_i \tilde{\Delta} \rho_o \tau^{-(2\ell+1)} \quad , \quad (13)$$

$$W = \left(\frac{\sigma_o \sigma_i}{[R_o R_i]^3} \right)^{\frac{1}{2}} \frac{(\ell - 1)\ell(\ell + 1)(\ell + 2)}{(2\ell + 1)\rho} \quad . \quad (14)$$

Note that the only dimensional quantity is W which has the dimension of frequency squared. We also note from equation (9) that our problem of solving for compound drop systems is now reduced to solving for the coupled harmonic oscillator.

From (9), the eigenvalues are given by

$$K = \frac{1}{2} \left(\frac{cm_i}{\tau^3} + \frac{m_o \tau^3}{\sigma} \right) \pm \sqrt{\frac{1}{4} \left(\frac{cm_i}{\tau^3} - \frac{m_o \tau^3}{\sigma} \right)^2 + 1} \quad , \quad (15)$$

so that the normal mode frequencies, ω_{\pm}^2 , are given by

$$\omega_{\pm}^2 = \frac{K}{J} W \quad . \quad (16)$$

From (9) and (15), we obtain the corresponding eigenvectors as

$$\frac{1}{\sigma} \begin{pmatrix} \delta R_o \\ \delta R_i \end{pmatrix}_{\pm} = \begin{pmatrix} \Delta_o \\ \Delta_i \end{pmatrix}_{\pm} = \frac{1}{d \pm \sqrt{d^2 + 1}} \quad (17)$$

where

$$d = \frac{1}{2} \left(\frac{m_o \tau^3}{\sigma} - \frac{cm_i}{\tau^3} \right) \quad . \quad (18)$$

It is important to note that the positive square root in (17) corresponds to the positive square root in (15). Consequently, for the normal mode with the higher frequency, the boundary oscillations are in-phase. We call this "+" mode the "bubble" mode and the lower frequency mode the "sloshing" mode. It follows from the orthogonality of eigenvectors that

$$\sigma \begin{pmatrix} \delta R_o \\ \delta R_i \end{pmatrix}_{+} = \frac{1}{\sigma} \begin{pmatrix} \delta R_o \\ \delta R_i \end{pmatrix}_{-}^{-1} \quad . \quad (19)$$

Thus, the relative boundary displacement of the sloshing mode is out of phase. The proof of this phenomenon was obtained from experiments in a neutral buoyancy tank and the results are shown in Figure 2.

Using equations (10) to (16), numerical values of the eigenfrequencies for various physical parameters can be readily obtained. Furthermore, simple expressions of several limiting cases as shown below can be deduced in a straightforward way.

(i) When the host is rigid (i.e., $\rho_0 = \infty$), the $\omega_- = 0$ and

$$\omega_{\pm}^2 = \frac{\sigma_1(\ell - 1)\ell(\ell + 1)(\ell + 2)[\tau^{2\ell+1} - \tau^{-(2\ell+1)}]}{\bar{R}_i^3 \{[\ell\rho + (\ell + 1)\rho_1]\tau^{2\ell+1} + (\ell + 1)(\rho - \rho_1)\tau^{-(2\ell+1)}\}} \quad (20)$$

(ii) When the core is rigid (i.e., $\rho_1 = \infty$), then $\omega_- = 0$, and

$$\omega_{+}^2 = \frac{\sigma_0(\ell - 1)\ell(\ell + 1)(\ell + 2)[\tau^{2\ell+1} - \tau^{-(2\ell+1)}]}{\bar{R}_0^3 \{[\ell\rho_0 + (\ell + 1)\rho]\tau^{2\ell+1} + \ell(\rho - \rho_0)\tau^{-(2\ell+1)}\}} \quad (21)$$

(iii) When the shell is very thin (i.e., $\tau = \sqrt{R_0/R_i} = 1$), then $\omega_- = 0$,

$$\omega_{+}^2 = \frac{(\sigma_0 + \sigma_1)(\ell - 1)\ell(\ell + 1)(\ell + 2)}{\bar{R}^3[\ell\rho_0 + (\ell + 1)\rho_1]} \quad (22)$$

Note that this is the same expression as that of a sample drop oscillating in a host fluid⁽²⁾ with its effective interfacial tension $\sigma_0 + \sigma_1$.

(iv) When the shell is very thick (i.e., $\tau \rightarrow \infty$), then we get

$$\omega_{+}^2 \rightarrow \frac{4\pi\sigma_1(\ell - 1)\ell(\ell + 1)(\ell + 2)}{3V_c[\ell\rho + (\ell + 1)\rho_1]} \quad (23)$$

and

$$\omega_{-}^2 \rightarrow \frac{4\pi\sigma_0(\ell - 1)\ell(\ell + 1)(\ell + 2)}{3V_s[\ell\rho_0 + (\ell + 1)\rho]} \quad (24)$$

where V_c and V_s are the core and the shell volumes respectively. Expressions (23) and (24) suggest that in this limit the "bubble" and "sloshing" modes are no longer coupled since each mode represents the simple drop oscillation as derived by Lamb.⁽²⁾

Eigenfrequencies for more general three fluid systems are shown in Figure 3 in which $V_T = V_c + V_s$, and $N_{s\pm} = \omega_{\pm}/\omega_s$ where ω_s is the frequency of a simple drop which is made out of a shell fluid of volume V_s . Note that the expression for ω_s^2 is the same as the expression given in equation (24). In this figure the upper five curves represent "bubble" modes for the specified values of ρ_1/ρ when $\rho_1 = \rho_0$, and the lower three curves represent corresponding "sloshing" modes. Experimental points taken in a neutral buoyancy tank show good agreement with the theoretical curves for $\rho_1/\rho = 1$ in this figure. Good agreement with the theoretical prediction was also demonstrated in another compound drop system in which the core was rigid. The results for the relative boundary displacements are shown in Figure 4. We see that the preliminary experimental results in this case also agree well with theory.

An interesting core centering phenomenon was observed in our neutral buoyancy experiments. Initially, a static compound drop was prepared so that the inner and outer boundary surfaces were non-concentric. However, as the drop began to oscillate in one of its normal mode frequencies (at $\ell = 2$), the two surfaces became concentric within the accuracy of our observation. Though this centering phenomenon takes place within a few cycles of oscillation, the centering force seems to depend, among other things, on the oscillation amplitude and the shell thickness. Within the approximations used in this paper, the positions of the core anywhere within the drop is neutrally stable. It is necessary to consider the next order of approximation to find the restoring forces responsible for the centering of the core and the shell. Work on the core centering phenomenon and more detailed description of the present work will be published elsewhere.

REFERENCES

1. L. D. Landaw and E. M. Lifshitz, Fluid Mechanics, (Pergamon Press, London), pp. 239.
2. H. Lamb, Hydrodynamics, Sixth Edition, Cambridge University Press, Reprinted by Dover, New York, 1945, pp. 475.

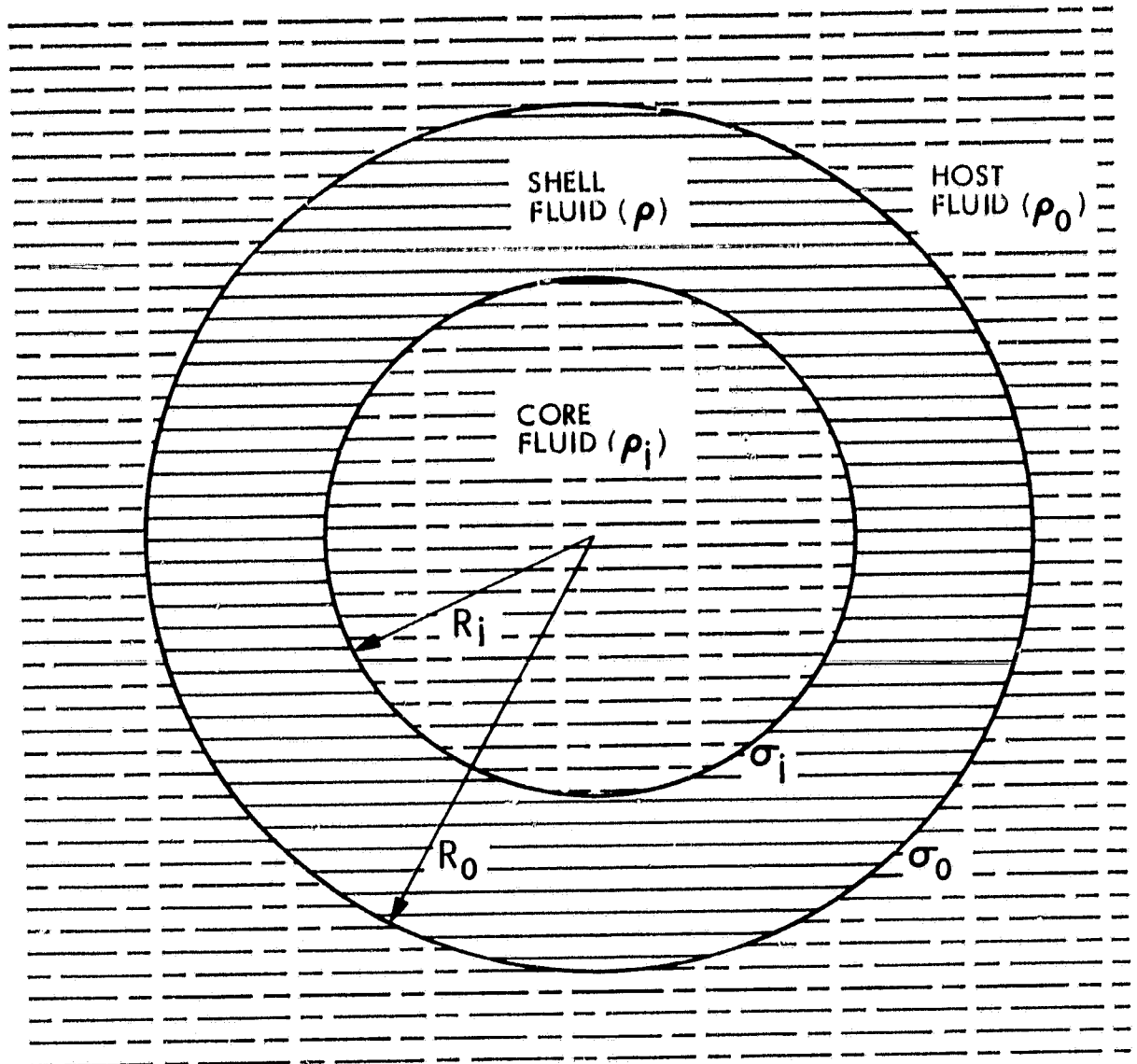


Figure 1. A concentric three fluid compound drop used in the theory.

ORIGINAL PAGE
BLACK AND WHITE PHOTOGRAPH

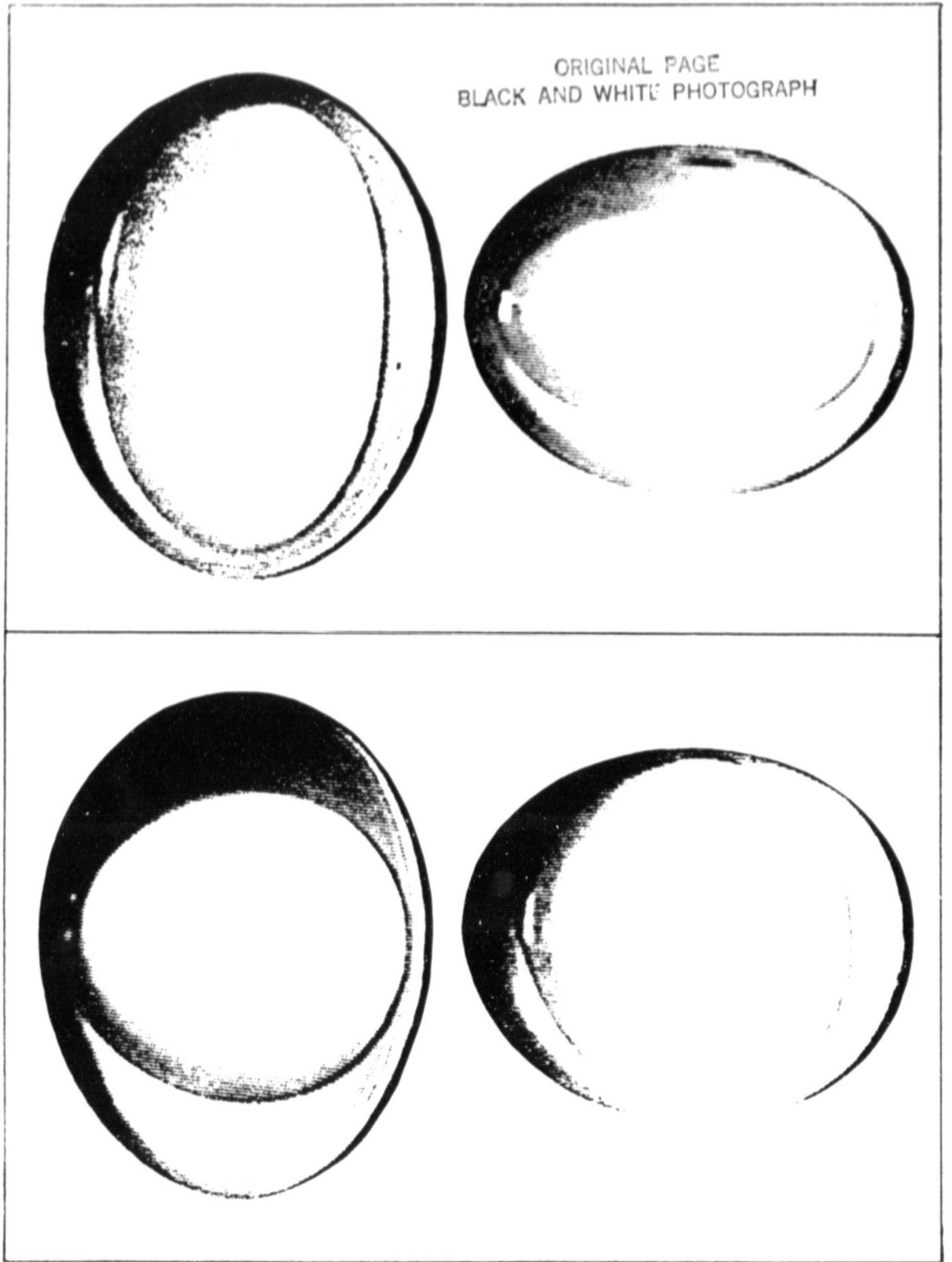


Figure 2. Bubble mode (top) and "sloshing" mode (bottom) oscillations of an oil-water-oil compound drop.

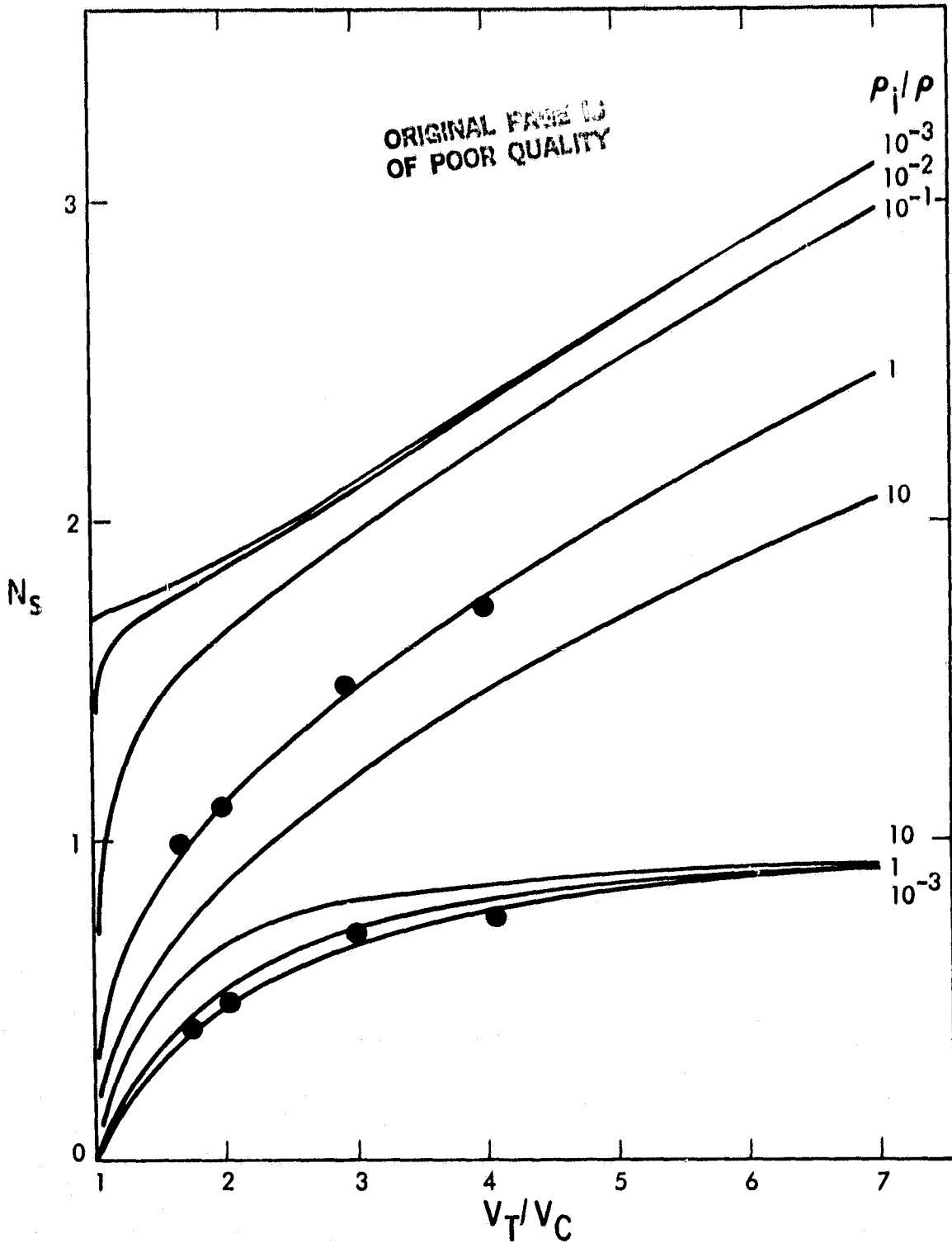


Figure 3. Normalized eigenfrequencies versus volume ratio of three fluid compound drop systems in which $p_i = p_o$ and ω_i and ω_o were maintained. The top five curves are for the "bubble" modes and the bottom three curves are for the corresponding "sloshing" modes. Experimental points are for the neutral buoyancy case.

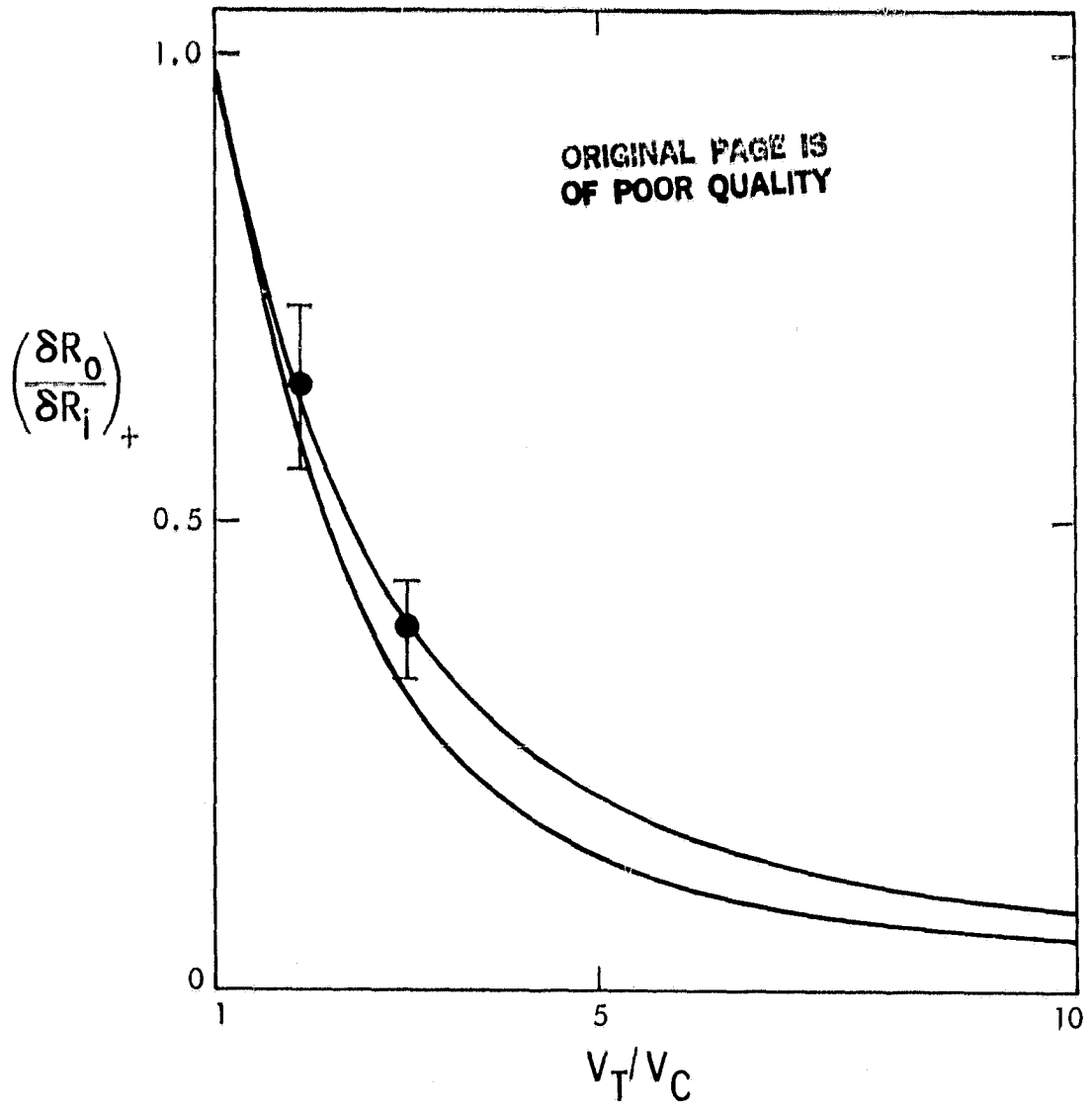


Figure 4. The ratio when $p_i = p_o$ and $\sigma_i = \sigma_o$. The top curve is for the air-water-air case ($p_i/p = 10^{-3}$), and the bottom curve and the data points are for the neutral buoyancy case.

IV. GROWTH OF ICE CRYSTALS FROM SALT SOLUTION IN LOW GRAVITY

Vernon Keller, Robert Owen, and Otha Vaughan, Jr.

PURPOSE

The objectives are to (1) determine whether or not the anomalously rapid ice crystal growth rates observed in supercooled dilute NaCl solution are caused by natural convection or crystal growth kinetics and (2) investigate the nature and magnitude of the natural convection around ice crystals growing from salt solution in low gravity.

Results from this study will enhance our knowledge of the poorly understood ice crystal growth mechanism. Since the growth mechanism and growth rate of ice crystals are important to areas of study as diverse as cryobiology, desalination of ice water by freezing, aircraft icing, and cloud physics, these results will be used by several scientific disciplines.

ACCOMPLISHMENTS

Ice crystals were nucleated and grown in both supercooled distilled water and supercooled salt solutions (0.5 to 6.0 percent NaCl) in the low-gravity environment available on the NASA KC-135 aircraft parabolic flights (Fig. IV-1). The crystal growth throughout a flight parabola (i.e., low gravity to high gravity to low gravity) was recorded photographically.

Our initial low-gravity experiments utilized a simple shadowgraph optical system. Results from these experiments indicated that the linear ice crystal growth rate in dilute salt solution is not strongly a function of natural convection. This is contrary to the conclusion of Vlahakis and Barduhn (1974)¹ who found that, for the same supercooling, ice crystals in the laboratory grew 2.5 times as fast in 0.5 percent NaCl solution as in distilled water and attributed this difference to enhanced convection in the salt solution. If their explanation were correct, then the linear crystal growth rate should change markedly as the crystal grows throughout a flight parabola. Furthermore, under low-gravity conditions the linear ice crystal growth rate in distilled water should be comparable or even greater than the growth rate in 0.5 percent NaCl solution at the same supercooling.

In our experiments, the linear ice crystal growth rate was not dramatically different between low gravity and high gravity. Our shadowgraph experiments also indicated that for the same supercooling the linear ice crystal growth rate is greater in 0.5 percent NaCl solution than in distilled water even when growth takes place in low gravity; i.e., anomalous growth occurs even in low gravity.

For the April and May 1981 low-gravity flights, we assembled a Moiré fringe optical system and integrated it with the existing hardware. The use of a sensitive optical system such as a Moiré system or a Mach-Zehnder interferometer system permits the observation of convection associated with the crystal growth. The Moiré

1. Vlahakis, J. G., and A. J. Barduhn, 1974: AICHE Journal, 20, No. 3, 581-591.

fringe system experiments demonstrate that convection around the growing crystals is greatly reduced in low gravity. In fact, within their limits of sensitivity, the Moiré experiments indicate that convection in the low-gravity flight parabolas is insufficient to overcome the adverse effects of the salt on the crystal growth kinetics. Together, these results support the conclusion that the anomalous growth rates cannot be explained on the basis of convection alone. Crystal growth kinetics must be considered.

CURRENT STATUS

Although we have successfully demonstrated with the Moiré fringe system that convection around ice crystals growing in 6.0 percent NaCl solution is substantially reduced in low gravity, a quantitative measurement of the convection velocity cannot be made with the present system. Furthermore, since only a short optical path length is presently available, the Moiré system has insufficient sensitivity to examine convection at such dilute salt concentrations as 1.0 percent NaCl or less - the precise regime where anomalous growth occurs.

As a solution to these problems, we have designed and are presently constructing a very sensitive Mach-Zehnder interferometer system. This system will be mounted on a special optically stable platform which will nearly double the optical path length available as well as inhibit vibration from the aircraft. The growth chamber is being modified to accommodate larger special antireflective-coated windows and to assure parallelism of the windows.

PLANNED FUTURE WORK

When assembly of the experiment hardware is complete, ground tests will be performed and the experiments will again be flown on the KC-135. The low-gravity data which results from flight of this hardware should demonstrate conclusively that the anomalous growth rates cannot be explained on the basis of convection alone. The data should also provide additional valuable information on the nature and magnitude of the natural convection associated with ice crystal growth from solution.

ACKNOWLEDGMENTS

The dedicated efforts of Robert Shurney, MSFC, Robert Williams, JSC, Lawrence Magers, JSC, and Pilots and crew of the KC-135 aircraft contributed immensely to this investigation.

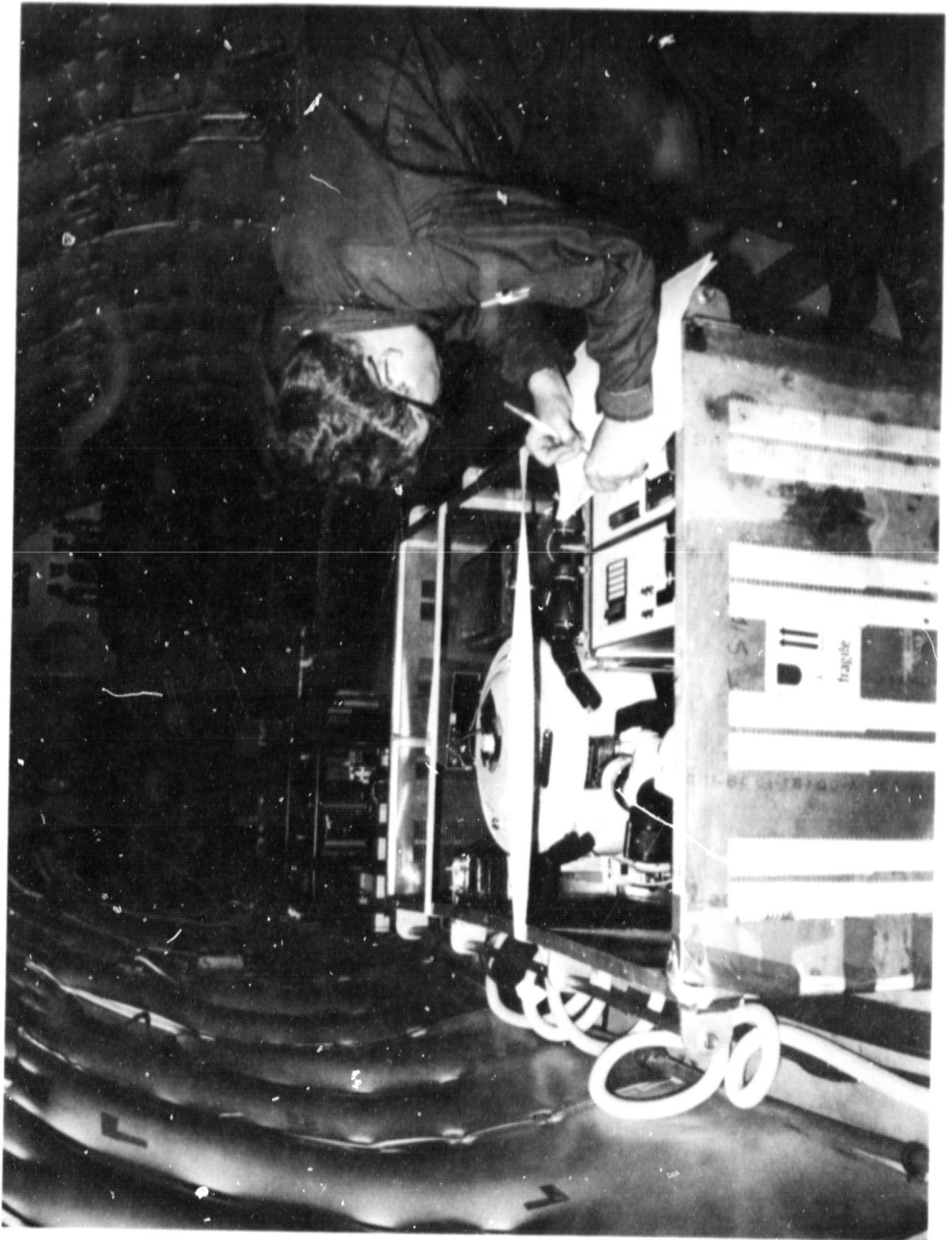


Figure IV-1. Experiment hardware for KC-135 flights.

V. THERMAL WAVE EXPERIMENT

B. J. Anderson, Vernon Keller, and David Bowdle

INTRODUCTION

The objective of this study is to generate and detect a controlled thermal wave in a cloud of water drops in low gravity, and to compare the results of this experiment with the results of a detailed, numerical, microphysical cloud model of this process. Thereby, the microphysics in the model can be verified and the mass accommodation coefficient for growing and evaporating drops (the fraction of impinging water vapor molecules which stick to the surface) can be estimated. Thus, these studies will allow measurements of fundamental microphysical properties of water droplets using low-gravity techniques which minimize the aberrations produced in previous measurements by sedimentation, convection, and supporting surfaces. Because the primary measurement is the location of the cloud/clear air interface, the difficult problem of measuring the radius or rate of change of radius of very small droplets is avoided in this study. Incorporation of these results into models of radiative transfer problems, fog formation and dispersal, and other processes occurring in dynamic, cloudy atmospheres, should significantly improve the predictability of these models. The low-gravity thermal wave technique should also permit similar studies of other multi-phase dispersions, such as phase separation in binary fluids.

RESEARCH METHOD

The primary element of the system is the experiment chamber (Fig. V-1a and V-1b); it is formed by a 5.1-cm diameter hole machined into the side of a solid aluminum cylinder, 25-cm diameter by 20-cm high. The thermal wave is generated by a 3- by 3-cm thermoelectric module (Borg-Warner, type 940-31) mounted to the side wall near the center of the cylinder. The cloud is illuminated by 30 degrees off-axis forward scattering and photographed with a motor-driven 35-mm Nikon camera at 1/3 magnification. The chamber walls are maintained wet by a charcoal-impregnated paper wick which remains black when moist. Double-pane windows assure thermal isolation from the outside environment, while "O" ring and gasket seals keep out the 70-mb pressure fluctuations during the parabolas. The unit is black anodized inside and out (Fig. V-2). The remainder of the equipment on the pallet consists of the electronics to drive the thermoelectric module and camera; illuminator; pump and air drier; aerosol generator; and miscellaneous small components. An accelerometer and multichannel chart recorder are flown on separate pallets.

The thermoelectric module is externally driven through a sinusoidal heating/cooling cycle centered on the dewpoint temperature of the air inside the chamber. As the thermal wave propagates outward from the thermoelectric module, water droplets nucleated from test aerosol particles alternately grow or evaporate. As Figure V-3 illustrates, the interface between the cloud and the clear air is clearly visible. The droplet cloud is photographed at 1-sec intervals. The droplet detection threshold for this system has been determined in the laboratory to be between 2- and 4- μm diameter.

PRECEDING PAGE BLANK NOT FILMED

ACCOMPLISHMENTS

The thermal wave chamber has been successfully flown on three series of low-gravity parabola flights on the NASA KC-135 aircraft. The initial test series (September 1980) demonstrated that a coherent thermal wave, with a sharply defined traveling interface between cloudy and non-cloudy air, can be generated in the test chamber and detected photographically. For the April and May 1981 flights, a Collision atomizer system was incorporated into the thermal wave equipment to provide a controlled method for introducing a known test aerosol - usually submicron polystyrene latex spheres. This aerosol generation system performed satisfactorily on both flight series. Several cloud formation events from these flights appeared to be suitable for comparison with theoretical models of droplet growth. Data analysis is now in progress.

The droplet growth model used in these studies is adapted from a detailed model of cloud microphysical processes originally developed for NASA's Atmospheric Cloud Physics Laboratory (ACPL). The ACPL model includes a time-dependent non-adiabatic option which treats droplet growth and evaporation, diffusion of heat and water vapor, and bulk air motion caused by temperature and pressure changes or gaseous concentration gradients. The non-adiabatic model is capable of simulating cloud formation/dissipation because of externally driven pressure changes and/or wall driven effects. Model geometry is presently limited to one-dimensional processes, with selectable (cartesian, cylindrical, or spherical) coordinate systems. The cartesian option has been employed thus far in these studies.

CONCLUSIONS

The work to date has clearly established the feasibility of this low-gravity method for studying the microphysics of the cloud formation process and the beginning of a good data base has been obtained. As expected, the need for several refinements in both the numerical model and the experimental method have been revealed since a satisfactory match between the two has not yet been obtained. A number of minor changes in the numerical model have already been implemented and the need for some additional work on the description of the boundary conditions has been indicated. On the hardware side, several additional measurements would be useful and the data recording method needs to be improved, as does the electronics for driving the thermoelectric module. At this stage in the experiment development, the aerosol generation and lighting and optics seem to be adequate. As the analysis of the results from the preliminary flights continue, it is expected that additional modifications to the hardware and model will be required before the quantitative results can be obtained. Overall, the experiment development is on schedule and no special problems are foreseen.

ORIGINAL PAGE IS
OF POOR QUALITY

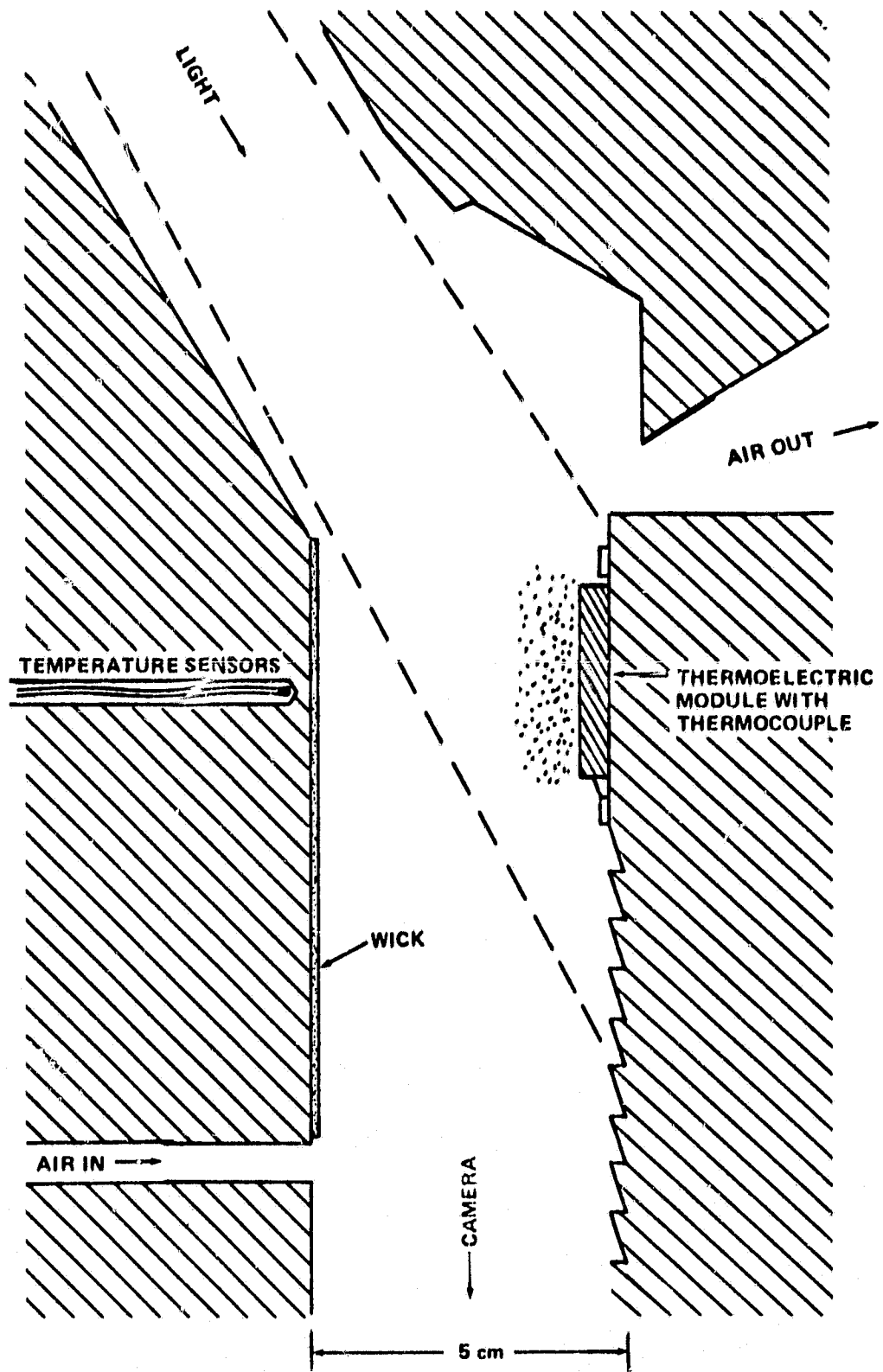


Figure V-1. Thermal wave chamber interior.

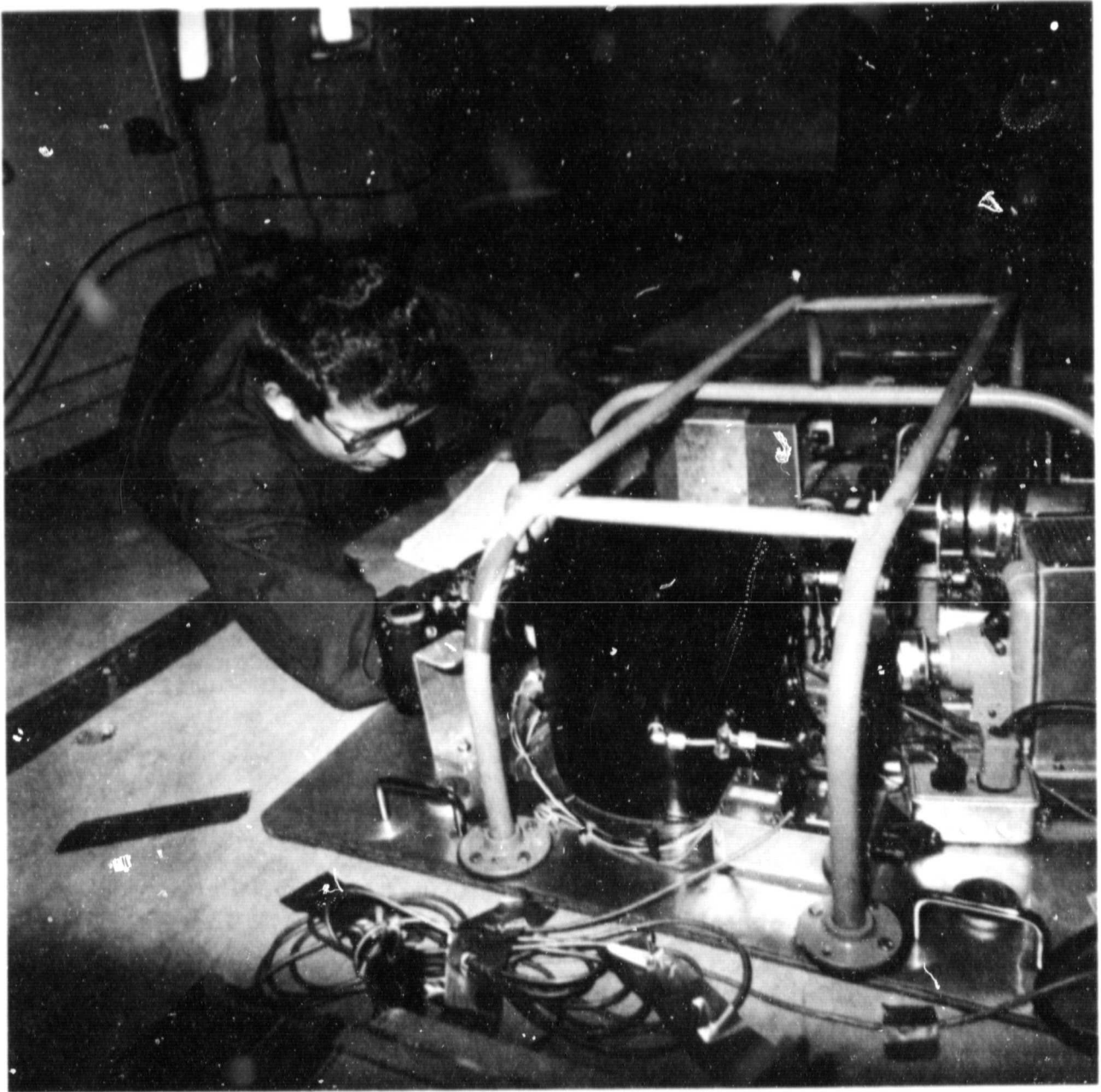


Figure V-2. Thermal wave experimental hardware for KC-135.

ORIGINAL PAGE
BLACK AND WHITE PHOTOGRAPH

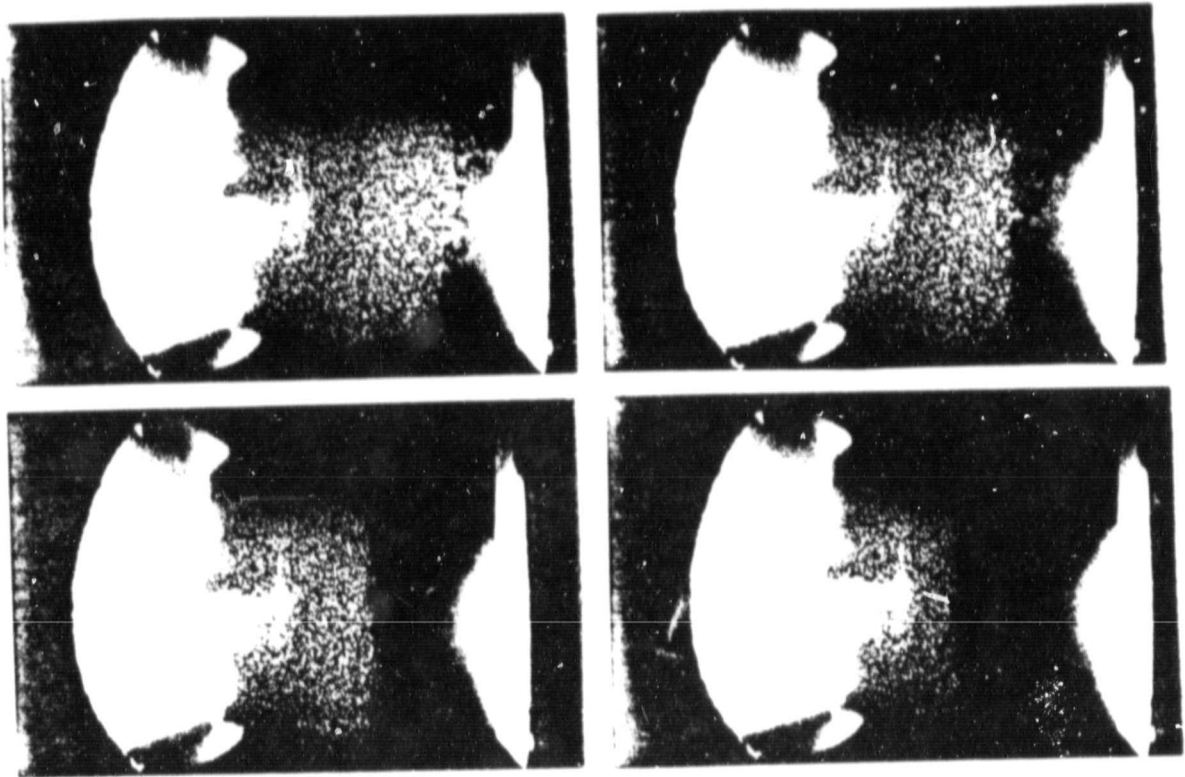


Figure V-3. A cloud evaporating in low gravity in response to the warming portion of the thermal wave. Note the well-defined interface and the lack of relative motion from frame to frame. Interval between photographs is 1 sec.

VI. OPTICAL MEASUREMENTS AND TESTS PERFORMED
IN A LOW-GRAVITY ENVIRONMENT

By Robert B. Owen

INTRODUCTION

Shadowgraph and schlieren optical systems useful in measuring fluid flow have been flown in the NASA KC-135 low-gravity simulation aircraft. The systems have been used to study gravity-related flow occurring during solidification from a cooled solution of ammonium chloride and water, in CoSO_4 electrodeposition solution, and in immiscible and crystal melt solutions. Critical optical system elements, such as lasers and spatial filters, have been tested in a low-gravity environment. System design, configuration, and performance are discussed, and some preliminary results are presented.

SYSTEM DESIGN

System Operational Environment

One of the major considerations in optical system design is the environment in which the system will be operated. The systems discussed herein were designed to function during low-gravity simulation missions on board the NASA KC-135 aircraft. A typical mission of two to three hours will consist of flying 30 to 40 low-gravity parabolas, each of which yields approximately 30 sec of low (1×10^{-2} g) gravity environment. A parabola profile is shown in Figure VI-1. The maneuvers can be flown consecutively, roller coaster fashion, or can be separated by sufficient time to alter the experiment.

The aircraft cargo area is essentially open, leaving a space approximately $18.3 \times 3.2 \times 2.0$ m for experimental use. The KC-135 interior is shown in Figure VI-2. Experimental packages can be either bolted to the aircraft floor or, if an effective gravitational force lower than 10^{-2} g is required, free floated inside the aircraft. However, a free-floating package is more limited in weight, power, and investigator interaction than is a bolted-down package. In order to allow adjustments to be made to the optics in low gravity, the current series of packages was bolted to the aircraft.

Electrical power is supplied by the KC-135, and gas and cryogenic systems are available. Cabin pressure and temperature are controlled during flight. However, the optical design must allow for potential loss of cabin pressure at altitude (40,000 ft), which would result in a pressure as low as 2.7 psia. In addition, as part of ground operations, the system is shipped to Houston, assembled and aligned in the aircraft hangar, loaded onto the aircraft by forklift, and, in general, subjected to various pressure, temperature, and vibration stresses. For safety reasons, the system must also be designed to withstand an 8 g crash load [1].

System Configurations

Laser Test System

This system was designed to monitor laser performance under low-gravity conditions. This test was necessary to verify that the lasers used in the shadowgraph/schlieren system described below would function normally in the environment of the KC-135 aircraft. The test configuration is shown in Figure VI-3. The system consists simply of a Spectra Physics Model 144 5 mW He-Ne gas laser, a United Detector Technology Model UDT-21A power meter, and a Linear Model 142 chart recorder. The power meter is all solid state with a digital readout and has a stability of 1 part in 10^3 for 1 hr. The chart recorder has a repeatability of ± 0.1 percent. The laser output was passed through a neutral density filter with an optical density of 3.0 to match the power meter's capacity. This test was also of interest because a gas laser will be used as the primary light source for the Fluids Experiment System experiment on the Space Shuttle. Since such lasers are usually operated in a 1-g environment in which normal convection occurs, the effects of a low-g environment on the laser plasma are unknown. The only previous gas laser operated in microgravity was that used for brief periods on the Pioneer Venus cloud particle size spectrometer [2], and no laser power measurements were made during that mission.

Laser power measurements were made by the author on a September 11, 1979, KC-135 flight. No fluctuation in laser output significantly above the noise level of the meter was observed during the low-g periods of the mission. The laser output increased by 1.4 percent during the course of the test. This variation was gradual and occurred over a period of approximately 1.5 hr; at no time were rapid variations observed in laser output. This slight change in laser output is quite reasonable, considering the variations in pressure, temperature, and vibration levels that the laser was subjected to during the flight, and is not related to low-g portions of the mission.

Further laser tests were conducted indirectly by operation of the laser shadowgraph/schlieren system on the KC-135. In particular, examination of the expanded beam following passage of the raw beam through the spatial filter revealed no fluctuations between low- and high-g operation. This test indicated that no significant multimoding was occurring in the laser. In addition, photographs taken of the expanded beam in both high- and low-g showed no lobe patterns. The flow patterns observed in low-g using the shadowgraph/schlieren system described below can therefore be interpreted in a straightforward manner. There is also no reason at this time to expect an initial variation in laser output due to low-g effects on the type of laser envisioned for use on the Fluids Experiment System. Possible long-term low-g effects are still unknown.

Laser Shadowgraph/Schlieren System

This system was designed to observe fluid flow under low-gravity conditions. The principles of operation for these techniques are well known [3] allowing straightforward data interpretation. The system was laid out in a standard schlieren Z configuration on a 0.9 m \times 1.2 m \times 0.635 cm thick steel slab containing an array of drilled and tapped holes on 2.54 cm centers. Use of this slab allowed components to be shifted as required for different setups. A system diagram is shown in Figure VI-4.

For reasons mentioned previously, extremely rugged optical components were chosen. All system elements were bolted to the slab which was, in turn, bolted to

the aircraft. The laser used was a Jodon HN-10, the spatial filter was a Spectra Physics Model 332, the collimator was a modified Tropel Model 280 laser collimator, the mirrors were Newport Research Corporation (NRC) DM.4 dielectric mirrors, and the schlieren lens was a Xenar 1:4.5/240. Various NRC mirror mounts, posts, bases, lab jacks, rotators, translators, platforms, and lens positioners were used to mount and align components, and the data were recorded on a Nikon 35 mm motor-driven camera with a 250 exposure film cassette. Pan-x film was used, and exposure times were set at 1/125 sec (schlieren) and 1/250 sec (shadowgraph). A system photograph is shown in Figure VI-5.

RESULTS

Observation of Flow During Solidification

The purpose of this experiment was to observe fluid flow during solidification of the metal model material $\text{NH}_4\text{Cl-H}_2\text{O}$. This flow is of interest in elucidation of casting mechanisms, an understanding of which would be useful in developing applications of space flight that will advance materials science and technology. This solution was employed for the study because it solidifies like a metallic alloy [4] and because its transparency allows direct observation of the solidification process. In this material system the fluid ahead of the interface is lighter than the initial fluid, causing the eruption of jet-like plumes. The phenomenon is associated with freckling in superalloys. The low-gravity environment was selected for the purpose of eliminating gravity-induced fluid flow effects. This solution has been previously photographed during solidification in the low (10^{-5} g) gravity environment of a sounding rocket [5,6], but no observations have been made of associated fluid flow.

The test sample was contained in a package previously developed for sounding rocket flights (Fig. VI-6), allowing the sample to be heated and cooled as required during the aircraft flights. The experiment was flown on July 12 and 13 and September 11, 12, and 13, 1979, in two series of KC-135 flights. The laser shadowgraph/schlieren system described previously was used as the optical measurement system. The growth plumes of interest were successfully observed and are shown in Figure VI-7. The measured flow rates are significantly less than had been expected from theoretical calculations [7] and have been discussed in detail elsewhere [8]. This experiment originated with, and was performed with, M. H. Johnston, NASA.

Observation of Electrodeposition Flow

The purpose of this experiment was to examine concentration gradients and flow in plating solutions subjected to a microgravity environment. These observations will help determine the extent to which larger neutral particles which cannot be readily suspended on Earth can be codeposited in low gravity with metals, possibly improving desirable material properties such as tensile strength, wear, and hardness. Co-CoSO₄ was selected as the deposition system because of its compatibility with the 6328 Å He-Ne laser used in the shadowgraph/schlieren system and because of its relatively low toxicity.

The CoSO_4 plating solution was contained in a $4.0 \times 4.5 \times 1.2$ cm fluorometric cell positioned in an aluminum holder which allowed for fixing the 1 cm^2 Co electrodes in either a vertical or horizontal configuration. The electrodeposition current was controlled by a variable resistance box and typically ranged from 20 to 30 mA.

Gaseous release in the cell was minimized by operating in a $\text{M-M}^{+n}\text{-M}$ mode (metal in and metal out).

The experiment was flown on May 14 and 15, 1980, on a series of KC-135 flights. The test cell was positioned with its plates vertical for one flight test series and horizontal for another, and 35 mm photographs were taken of the resulting concentration gradients and flows. The optical system was operated in the shadowgraph mode only, since ground studies had shown that mode to be optimum for this experiment. Initial examination of the flight photographs shows a significant decrease in flow while under low-gravity conditions, as can be seen in Figure VI-8.

The electrodeposition test cell concept, design, and construction originated with Gordon Fisher, Inco Research and Development Center, and Clyde Riley and H. Dwain Coble, The University of Alabama in Huntsville.

Observations of Immiscible and Crystal Melt Solutions

As part of the checkout of the laser shadowgraph/schlieren system, observations were made in low gravity of immiscible and crystal melt solutions. Some typical results are shown in Figures VI-9 and VI-10. These photographs were taken during a September 13, 1979, KC-135 flight.

Other Hardware Tests

Indirect hardware tests were conducted as part of the evaluation of the performance of the laser shadowgraph/schlieren system in a low-g environment. In each KC-135 flight series, improvements were made in system components, resulting in increased reliability, versatility, and ease of operation. One particularly critical hardware item was the spatial filter. Full use of this component required that the laser beam be aligned to pass through a 3 micron pinhole. On early flights the load applied to this component when the aircraft passed from the 2-g pullout to the low-g parabola ruined the system alignment and necessitated removal of the pinhole. After several flights and several changes, the spatial filter assembly was mounted in a modified NRC Model 600 A-2 optical mount which proved to be quite adequate for low-gravity work. This mount was rugged, easy to reinforce, and could be adjusted during flight. Use of the spatial filter resulted in a cleaner, better defined image than had been obtained on previous flights. These hardware tests are resulting in improved optical system designs for not only KC-135 flights, but also for flight packages scheduled for F-104 aircraft and Space Shuttle flights.

SUMMARY

The design and configuration of optical systems used to make gravity-related fluid flow measurements on board the NASA KC-135 low-gravity simulation aircraft have been presented. These systems have successfully measured flows in cooled and

solidified ammonium chloride and water, electroplated cobalt in CoSO_4 solution, and immiscible and crystal melt solutions. Further tests are planned on the KC-135, both with additional test samples and with more advanced optical systems.

ACKNOWLEDGMENTS

The author acknowledges the aid and cooperation of Robert E. Shurney, MSFC; Donald Griggs, JSC; Lawrence M. Magers, JSC; and the KC-135 pilots and ground crew.

REFERENCES

1. Simulation Program, Man/Systems Simulation User's Manual, Revision 1, Man/Systems Integration Branch, Operations Development Division, Systems Analysis and Integration Laboratory, Marshall Space Flight Center, NASA, April 20, 1976.
2. R. G. Knollenberg and D. M. Hunten, *Science* 203, 1979, pp. 792-795.
3. L. A. Vasil'ev: *Schlieren Methods*. Keter Publishers Ltd., London, 1971.
4. K. A. Jackson and J. D. Hunt: *Acta Met.* 13, 1965, p. 1212.
5. M. H. Johnston and C. S. Griner: *Met Trans.* 8A, 1977, pp. 77-82.
6. M. H. Johnston, C. S. Griner, R. A. Parr, and S. J. Robertson: *J. Crystal Growth*, 50, 1980, pp. 831-838.
7. S. J. Robertson: *Thermal and Fluid Flow Analysis of Sounding Rocket Experiments 74-21/2R and 74-21/3R*. Lockheed Report LMSC-HREC TR D568959, April 1979.
8. M. H. Johnston and R. B. Owen: *Proc. of the 157th Meeting of the Electrochemical Soc.* 80(1), 1980, pp. 1308-1309.

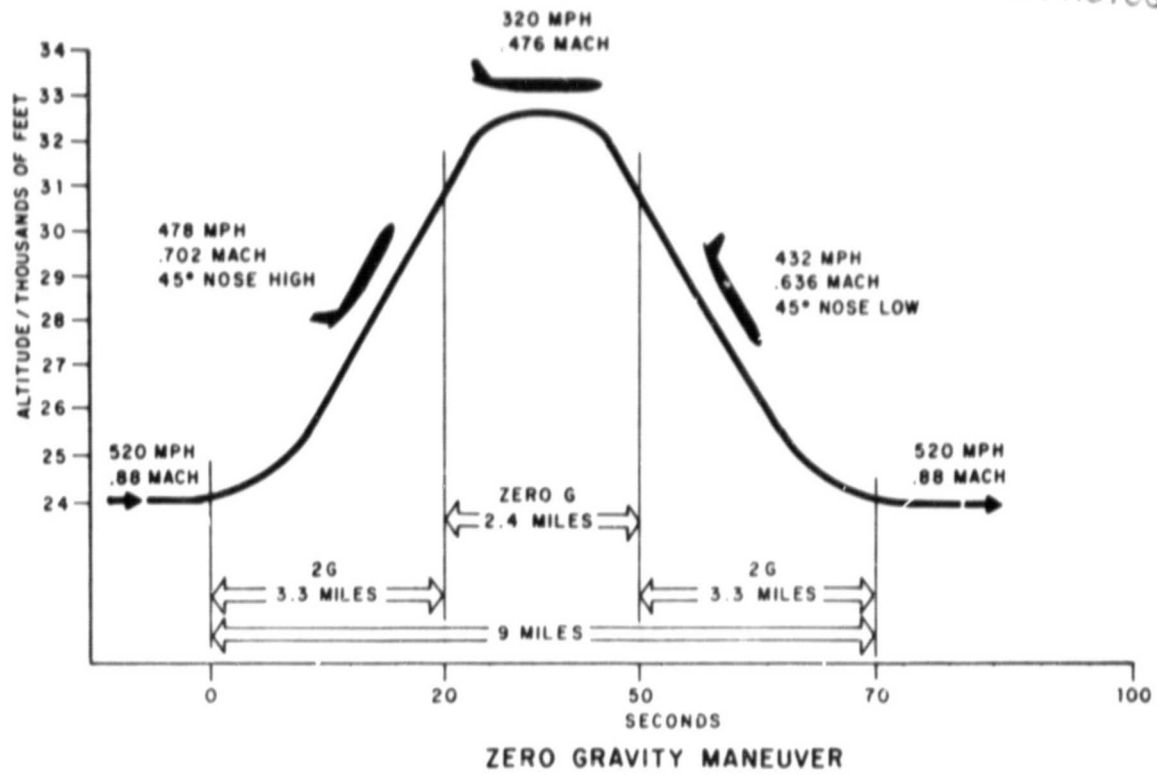


Figure VI-1. Flight parabola of KC-135 low-gravity simulation aircraft.



Figure VI-2. Interior of KC-135 low-gravity aircraft.

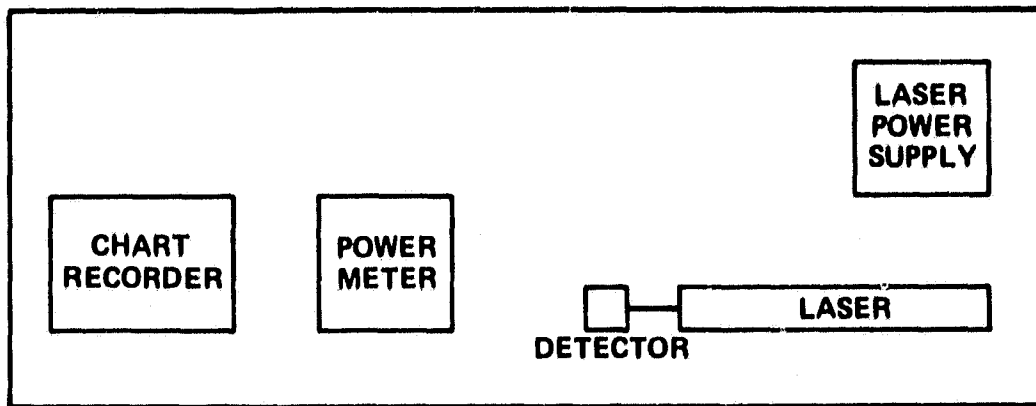


Figure VI-3. Laser power monitor configuration.

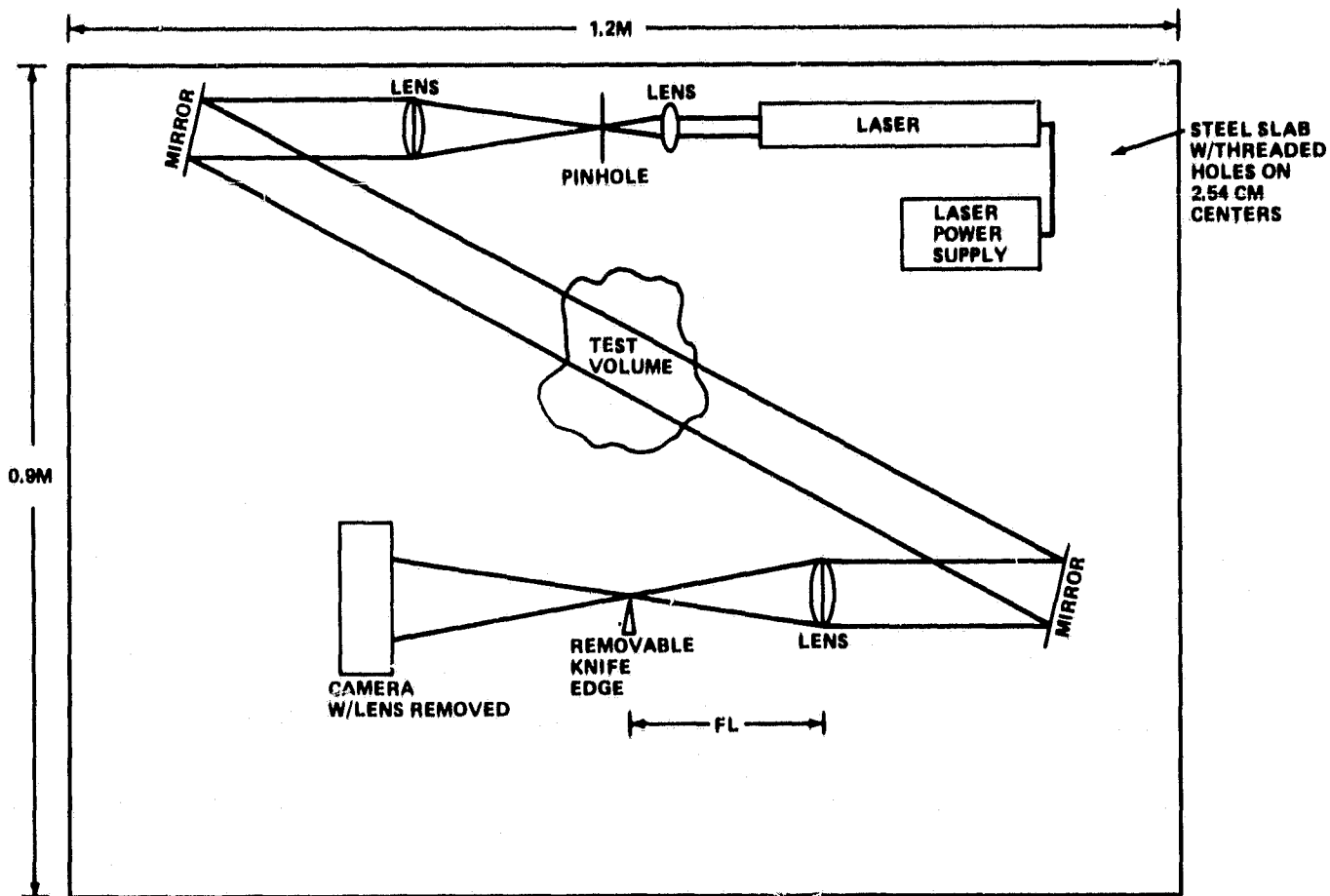


Figure VI-4. Laser shadowgraph/schlieren system configuration.

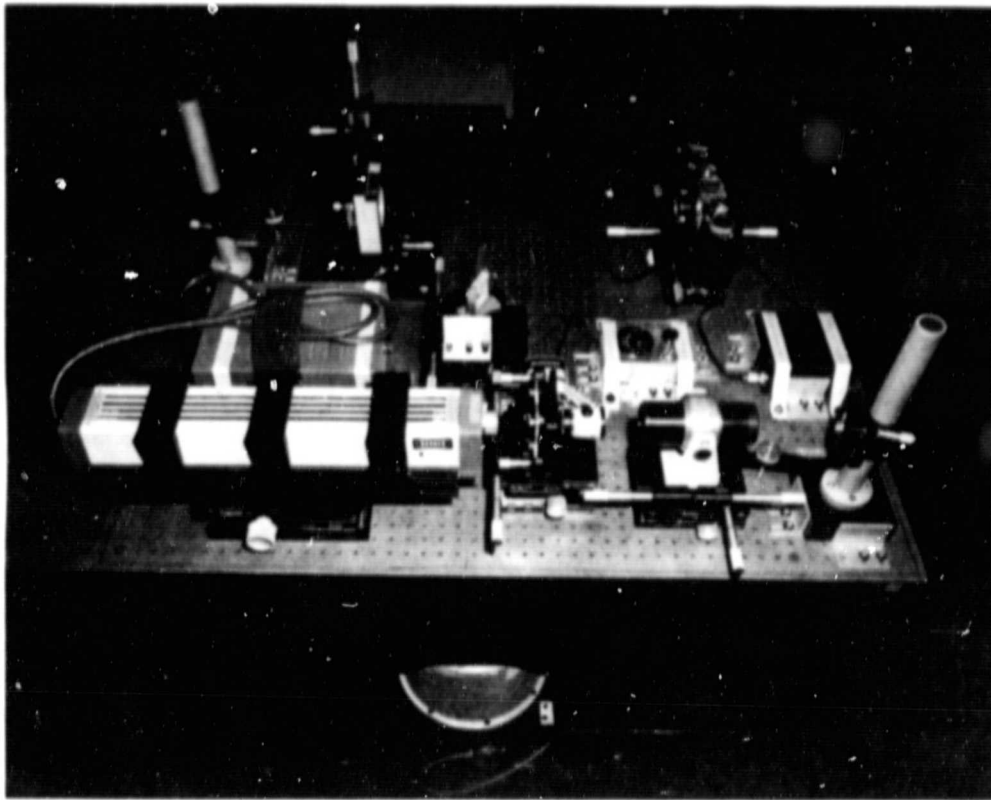


Figure VI-5. Laser shadowgraph/schlieren flight system.

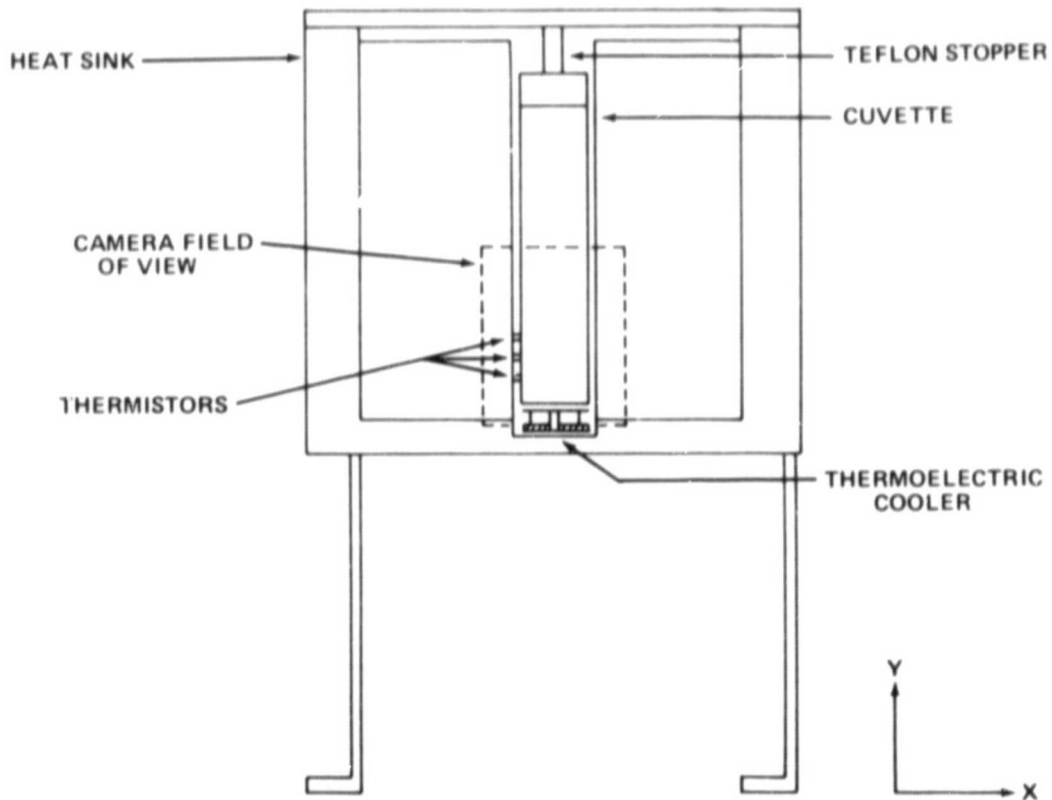


Figure VI-6. Cuvette assembly viewed along z-axis.

ORIGINAL PAGE
BLACK AND WHITE PHOTOGRAPH



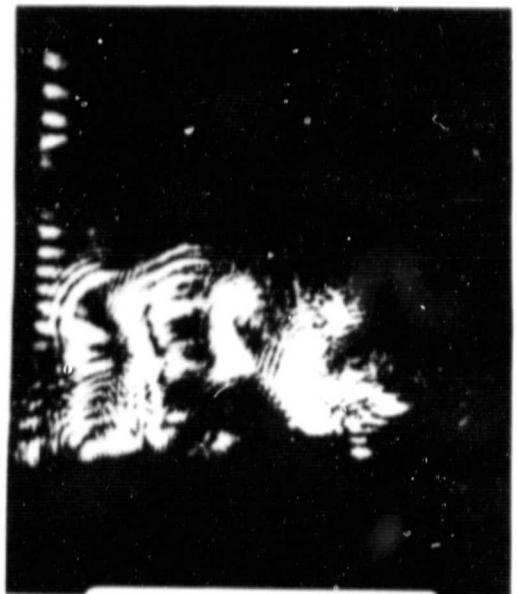
NORMAL LIGHTING



SHADOWGRAPH



SCHLIEREN, KNIFE EDGE IRRADIATION



SCHLIEREN, KNIFE EDGE IRRADIATION

$\text{Ni}_3\text{Ti}/\text{Ti}$ SOLIDIFICATION

Figure VI-7. Composite photograph of low gravity solidification.

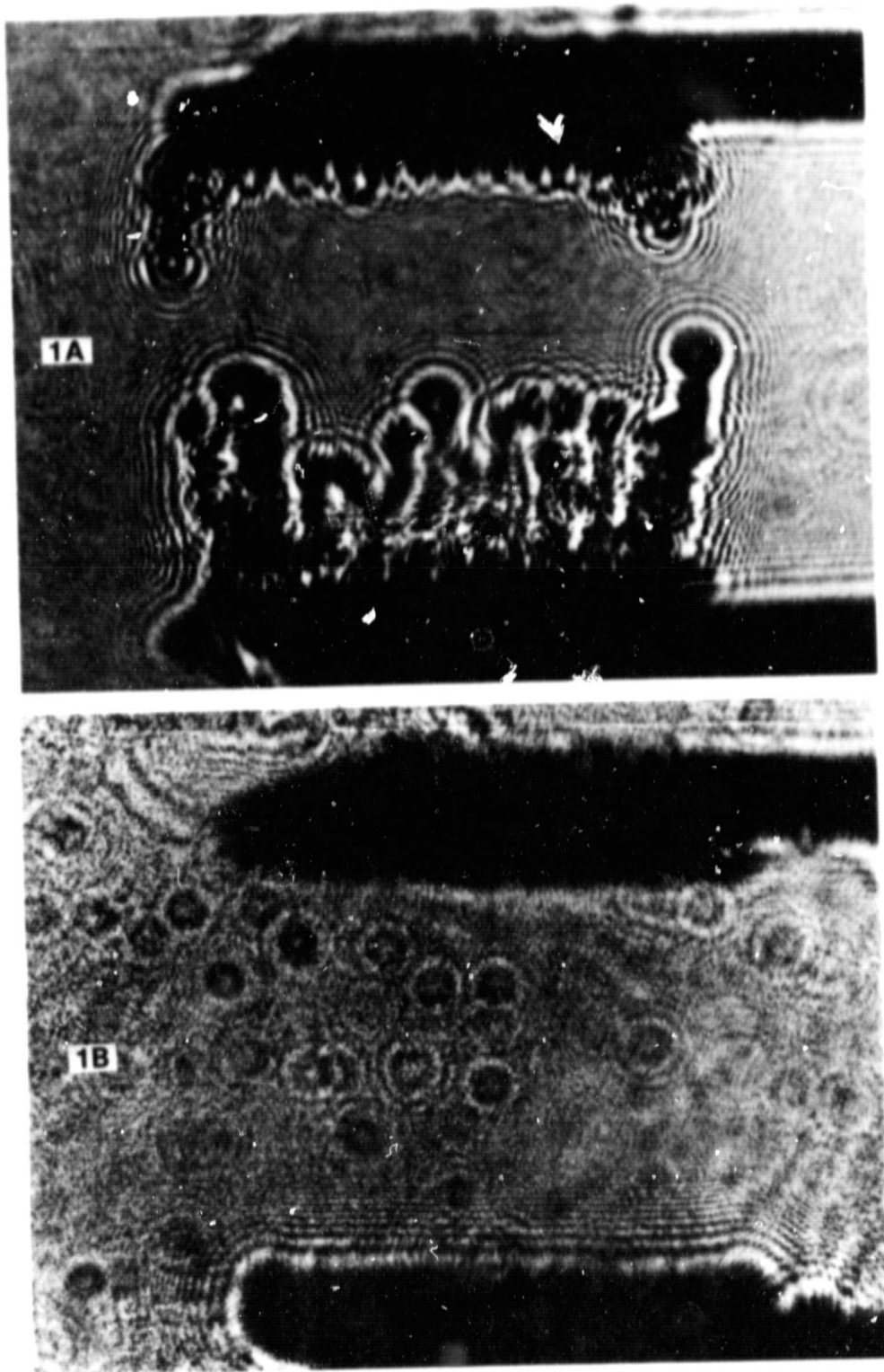


Figure VI-8. Comparison of convection under different gravity conditions. 1A shows convection density patterns building with horizontal electrodes (anode over cathode). 1B shows the lack of convection patterns in low gravity when all other conditions are identical, including time.

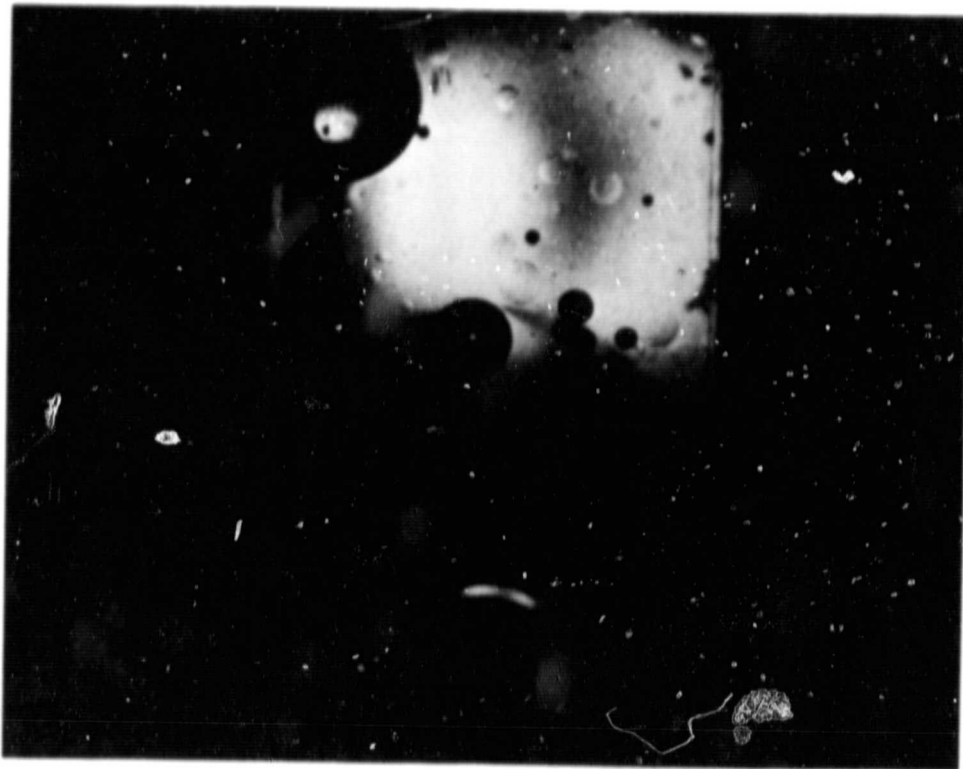


Figure VI-9. Immiscible solution in low gravity environment.

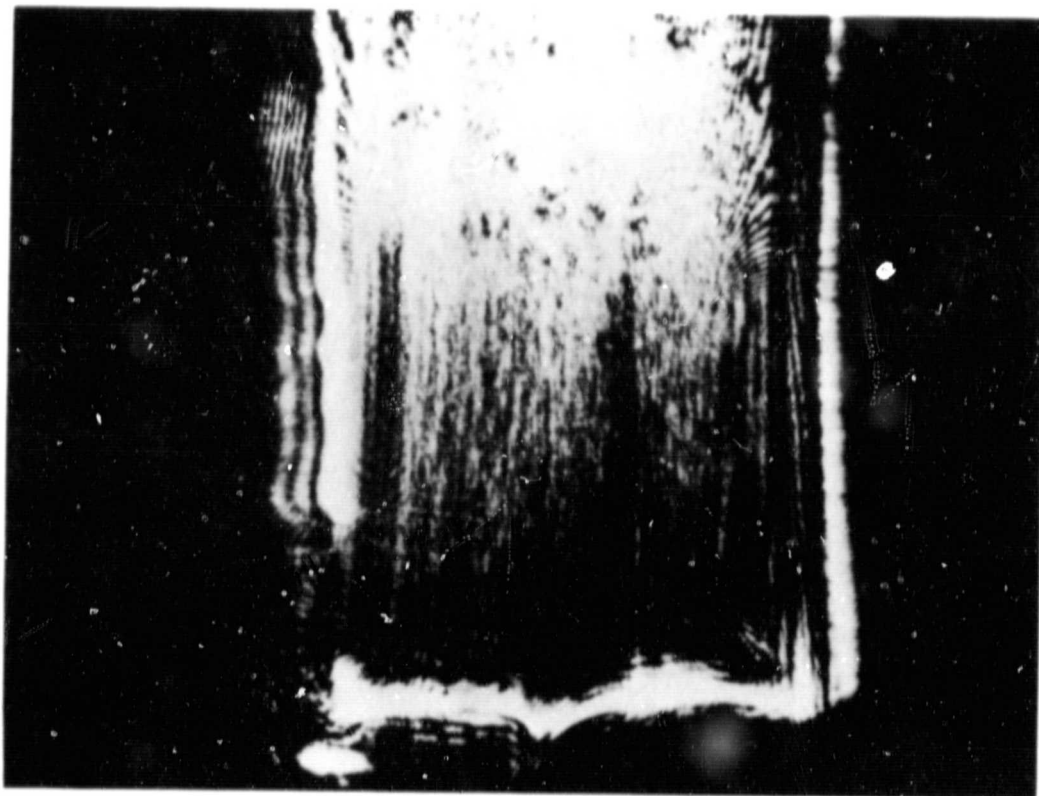


Figure VI-10. Crystal melt solution (TGS) in low gravity environment.

VII. HIGH TEMPERATURE CASTING FURNACE

By M. H. Johnston

One-cm diameter by 1- $\frac{1}{4}$ -cm slugs of ductile cast iron and Al-4.5Cu were placed in high purity alumina crucibles. To prevent excessive loss of the iron samples constituents the iron samples were surrounded by glass beads and then covered with an alumina lid. In all cases the lids were glued on to prevent the material escaping during low gravity.

In the second series of flights a thermocouple was placed in the base of the sample to provide temperature profiles. In order to determine which could best survive the high temperature molten metal environment, both pt-13 percent rh and chromel-alumel thermocouples were used.

The crucible holder configuration (Fig. VII-1) consists of an alumina tube with thermocouple and a threaded bolt at the base. After inserting the crucible in the crucible holder, it was wired into position and the entire assembly bolted into the furnace cannister.

The furnace cannister (Fig. VII-2A, VII-2B, VII-2C) contains five crucible holders for one series of experimental runs. The furnace is placed sequentially over the crucible holders. When the sample has been soaked at temperature for the required time period, the furnace is removed, placed on the next sample, and a quench cup is lowered over the hot crucible. Nitrogen gas is then blown around the crucible holder in order to solidify the sample during the allotted time period.

The gravity force was measured by accelerometers placed along three axes. The values of gravity level and temperature were recorded on a hot-pen stylus recorder.

In the second series of tests it was decided to solidify three of the samples on the plane during the low-g period and two samples during level flight for ground-based comparisons. All of the samples will then have seen similar external temperature, pressure, and humidity during processing.

The aluminum samples were processed at a furnace temperature of 800°C. The cast iron furnace temperature ranged from 1250° to 1480°C. The variation was caused by problems with thermocouples and furnace element failures.

The analysis of the first sets of aluminum and cast iron samples was begun in M&P Laboratory at MSFC. After being removed from the crucible holders, the samples were sliced along the central axis, mounted with diethyl phthalate molding resin, and polished with successively smaller grades of paper down to 600 grit. They were then polished with grade 9 diamond compound and 5 micron alumina. The structures became evident after etching. Figures VII-3 and VII-4 show cross sections of the first set of aluminum samples; Figures VII-5 and VII-6 show cross sections of the cast iron samples. These and all of the samples from the second series of flights were turned over to TRW and John Deere & Co. The results of their analyses have not yet been received.

ORIGINAL PAGE IS
OF POOR QUALITY

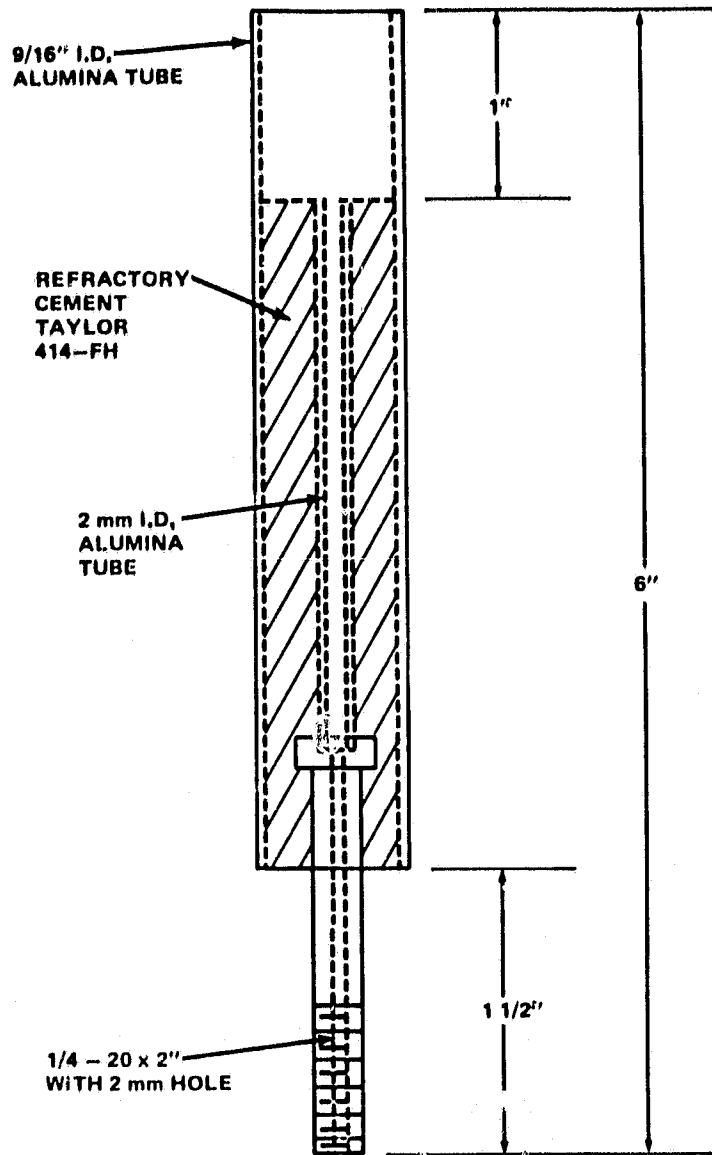


Figure VII-1. Sample containment crucible.

ORIGINAL PAGE IS
OF POOR QUALITY

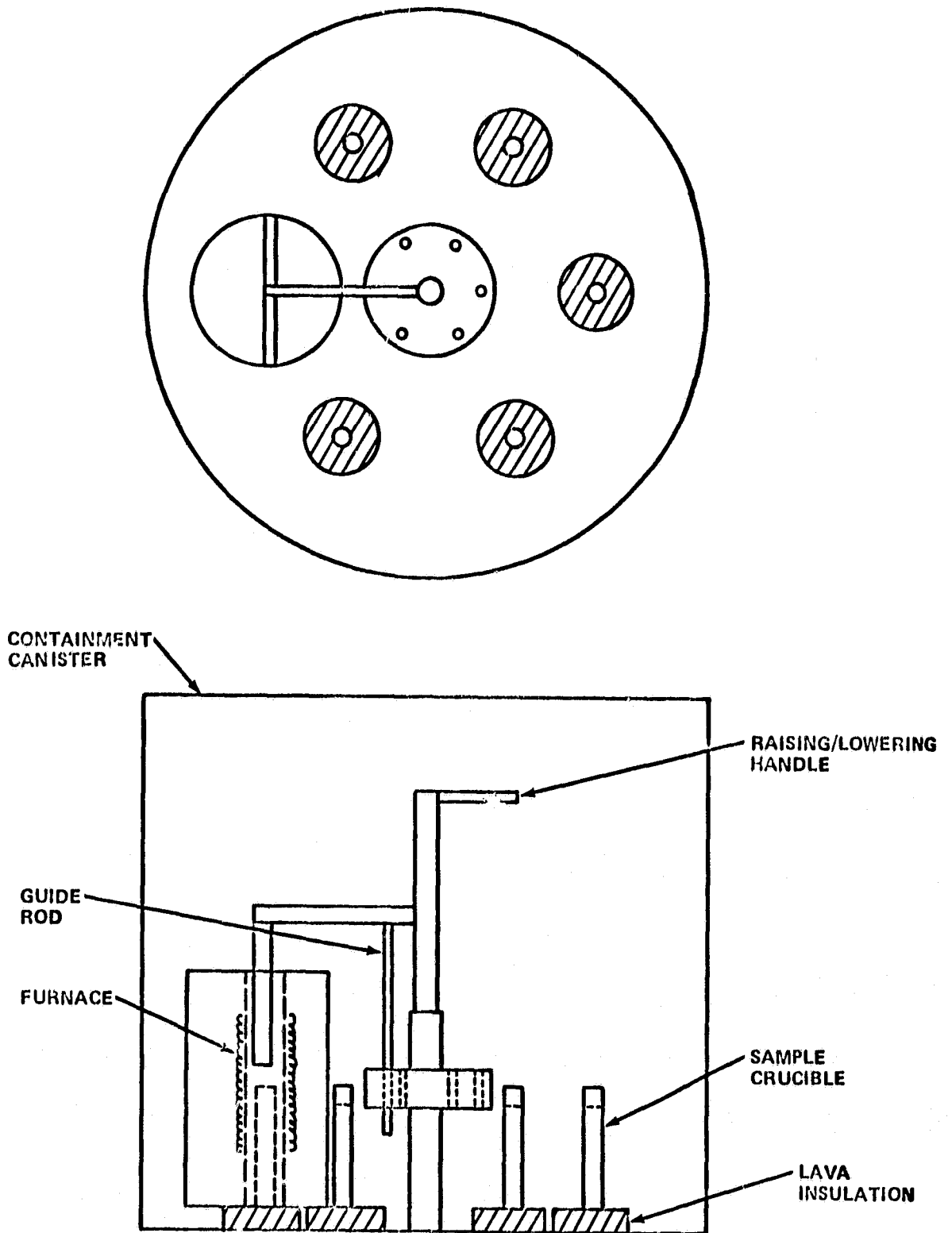


Figure VII-2A. KC-135 casting furnace assembly.



Figure VII-2B. KC-135 casting furnace assembly.



Figure VII-2C. KC-135 casting furnace operation.

ORIGINAL PAGE
BLACK AND WHITE PHOTOGRAPH

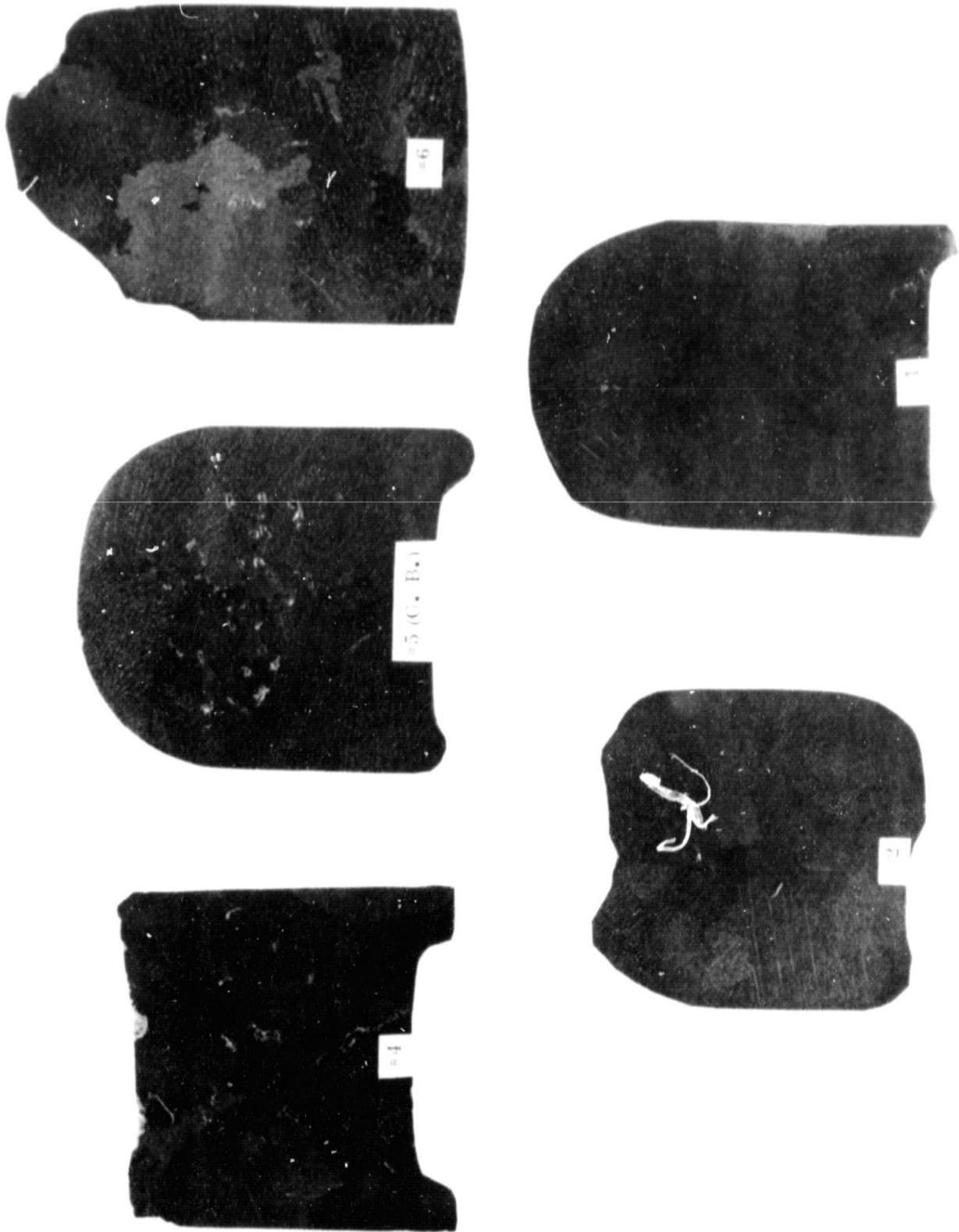


Figure VII-3. Al-4.5Cu samples processed on KC-135 airplane.

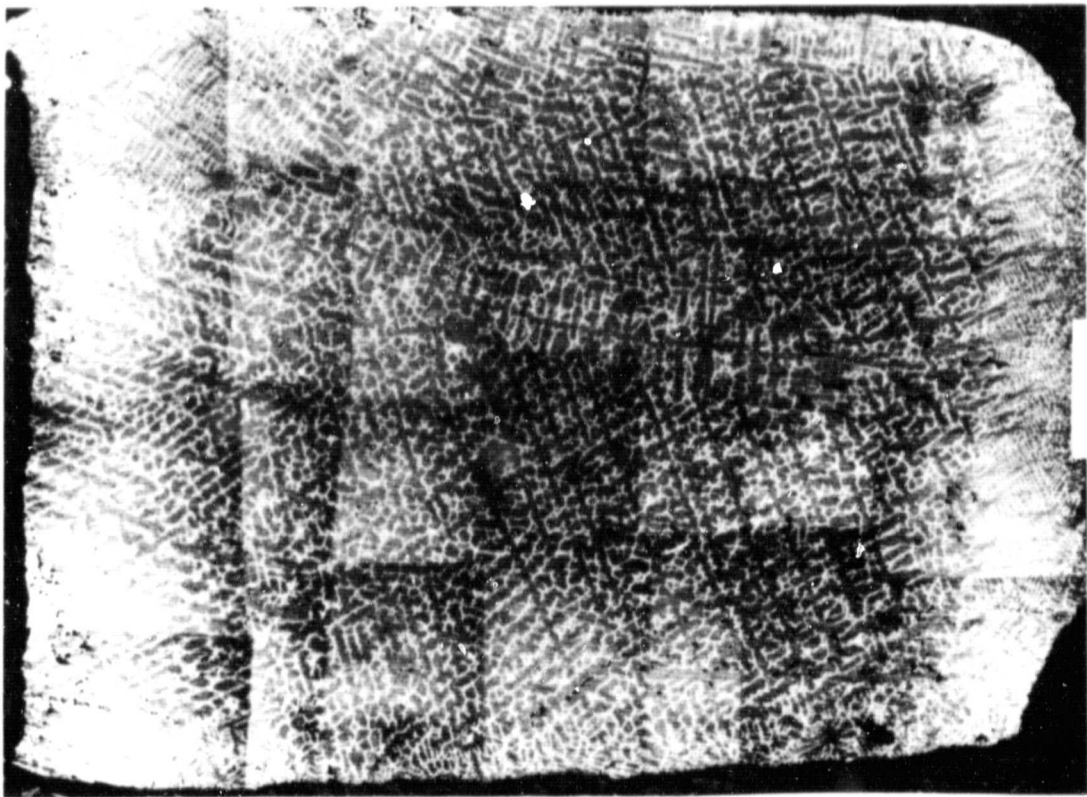
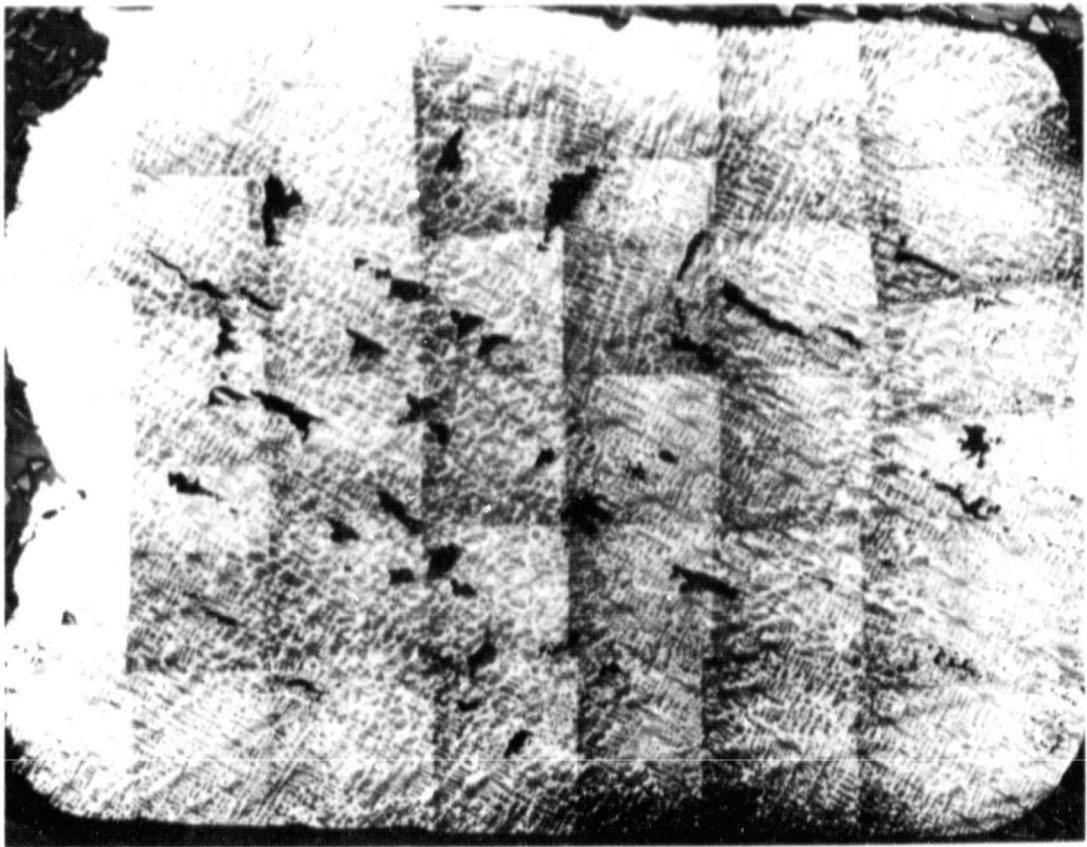
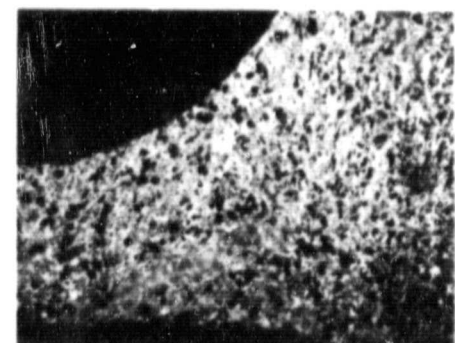
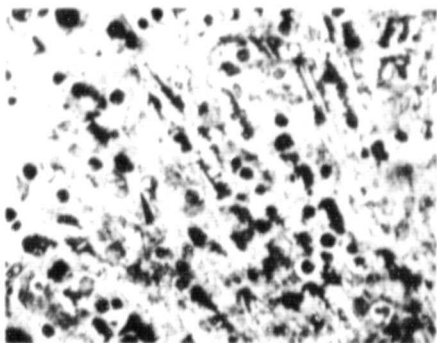
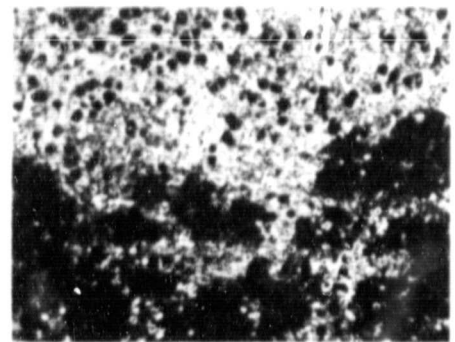
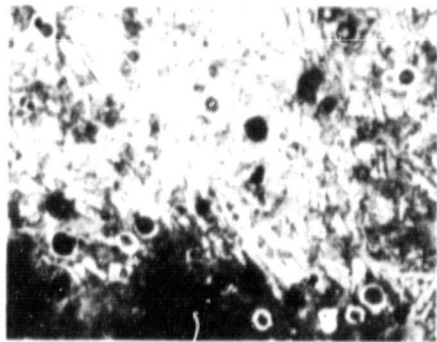
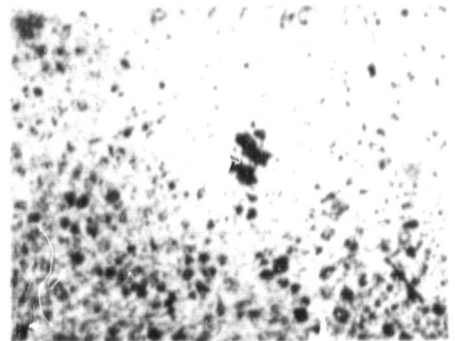
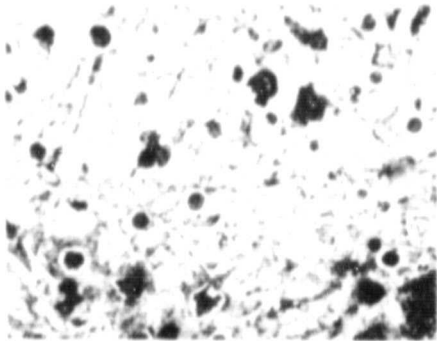
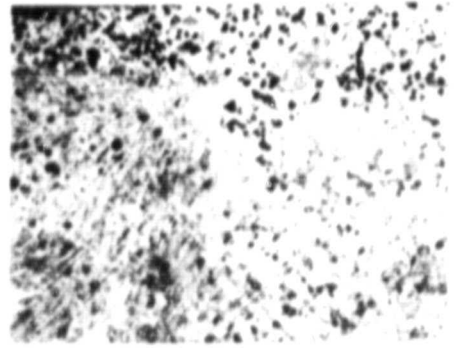
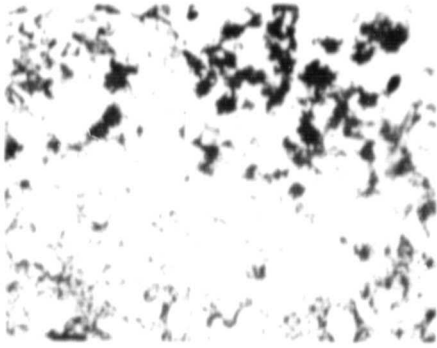


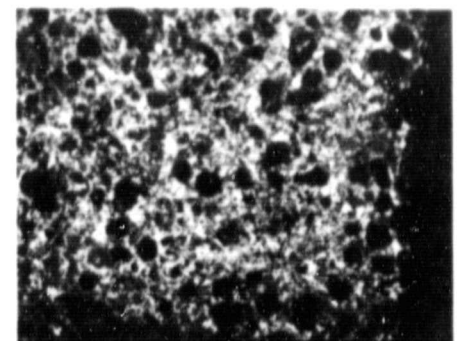
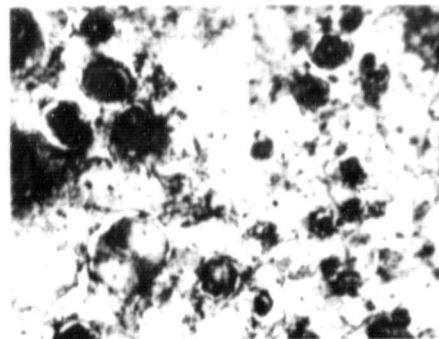
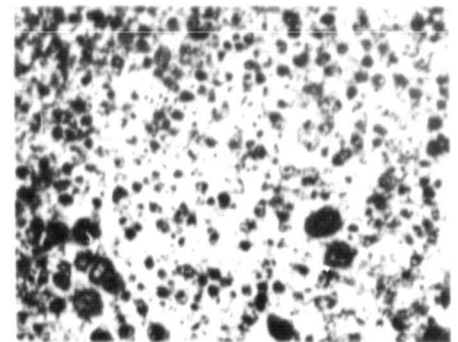
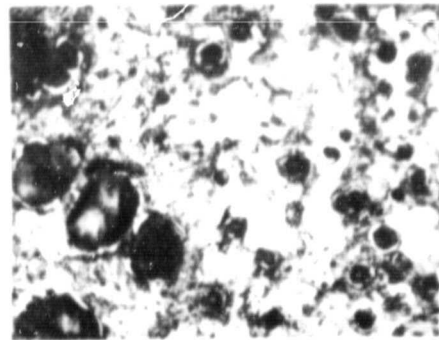
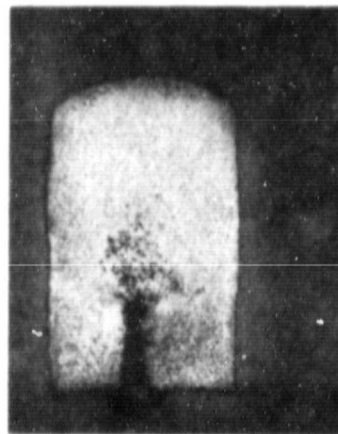
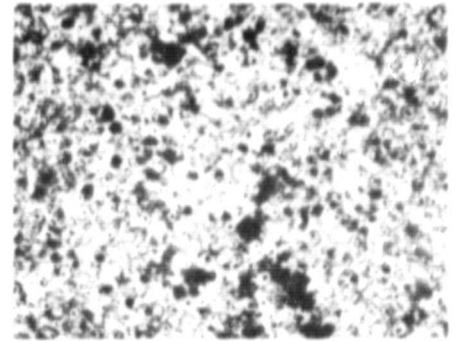
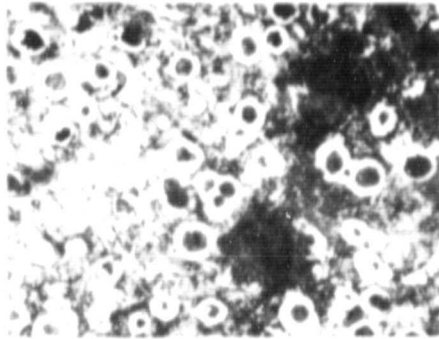
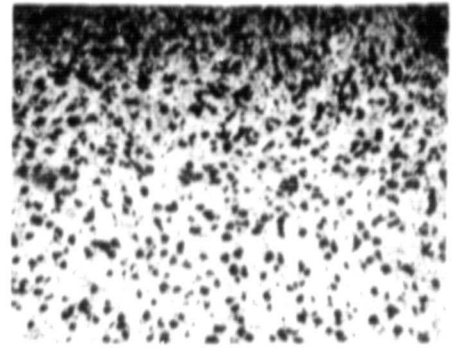
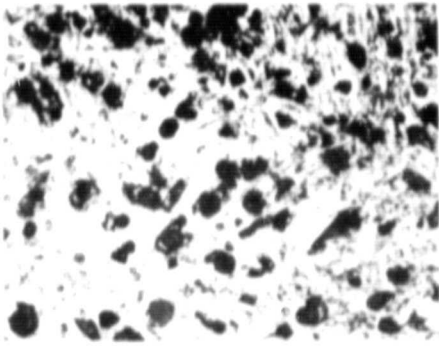
Figure VII-4. Al-4.5Cu ground base and KC-135 sample.



5X

CAST IRON SAMPLE FLOWN DURING MAY 1981, DAY 2 - RUN 2, SERIAL ETCB

Figure VII-5. KC-135 flight cast iron (day 2, run 2).



CAST IRON SAMPLE FLOWS DURING MAY 1951, DAY 3 - RUN 3, SEAL ETC.

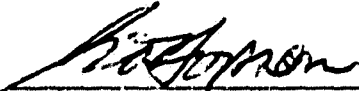
Figure VII-6. KC-135 flight cast iron (day 3, run 3).

APPROVAL

THE MARSHALL SPACE FLIGHT CENTER KC-135 ZERO GRAVITY
TEST PROGRAM FOR FY1981

By R. E. Shurney

The information in this report has been reviewed for technical content. This report, in its entirety, has been determined to be unclassified.



G. D. Hopson
Director, Systems Analysis
and Integration Laboratory